Received: 27 July 2020 | Revised: 5 November 2020 | Accepted: 12 November 2020

DOI: 10.1111/bre.12528

RESEARCH ARTICLE

Basin Research IAS EAGE WILEY

The structural evolution of pull-apart basins in response to changes in plate motion

Georgios-Pavlos Farangitakis[1] | **Ken J. W. McCaffrey**[1] | **Ernst Willingshofer**[2] | **Mark B. Allen**[1] | **Lara M. Kalnins**[3] | **Jeroen van Hunen**[1] | **Patricia Persaud**[4] | **Dimitrios Sokoutis**[2,5]

[1]Department of Earth Sciences, Durham University, Durham, United Kingdom

[2]Department of Earth Sciences, Utrecht University, Utrecht, the Netherlands

[3]School of GeoSciences, University of Edinburgh, Edinburgh, United Kingdom

[4]Department of Geology and Geophysics, Louisiana State University, Baton Rouge, LA, USA

[5]Department of Geosciences, University of Oslo, Oslo, Norway

Correspondence
Georgios-Pavlos Farangitakis, Department of Earth Sciences, Durham University, Durham, United Kingdom.
Email: georgios-pavlos.farangitakis@durham.ac.uk

Funding information
Royal Society of Edinburgh; UK Research and Innovation, Grant/Award Number: NEM00578X/1

Abstract

Pull-apart basins are structural features linked to the interactions between strike-slip and extensional tectonics. Their morphology and structural evolution are determined by factors such as extension rate, the basin length/width ratio, and changes in extension direction. In this work, we investigate the effect of a change in the plate motion direction on a pull-apart basin's structure, using analogue modelling experiments with a two-layer ductile-brittle configuration to simulate continental crust rheology. We initially impose orthogonal extension on an interconnected rift and strike-slip system to drive pull-apart development. Subsequently, we rotate the relative motion vector, imposing transtensional deformation and continuing with this new relative motion vector to the end of the experiment. To compare with natural examples, we analyse the model using seismic interpretation software, generating 3D fault structure and sedimentary thickness interpretations. Results show that the change in the direction of plate motion produces map-view sigmoidal oblique slip faults that become normal-slip when deformation adjusts to the new plate motion vector. Furthermore, sediment distribution is strongly influenced by the relative plate rotation, changing the locus of deposition inside the basin at each model stage. Finally, we compare our observations to seismic reflection images, sedimentary package thicknesses and fault interpretations from the Northern Gulf of California and find good agreement between model and nature. Similar fault arrays occur in the Bohai Basin in northern China, which suggests a rotational component in its evolution. More broadly, such similar structures could indicate a role for oblique extension and fault rotation in any pull-apart basin.

KEYWORDS

extension, plate motion changes, pull-apart basins, strike-slip, transtension

1 | INTRODUCTION

Pull-apart basins are structural depressions attributed to the presence of extensional features along strike-slip fault systems, found at releasing bends or steps (Rahe et al., 1998). They were first described in the Death Valley strike-slip fault system by Burchfiel and Stewart (1966), where they observed an oblique 'pulling-apart' of the two sides of the valley due to an oblique slip segment in the Death Valley Fault Zone. In their global catalogue of releasing and restraining bends on strike-slip systems, Mann (2007) documented around 150 such examples of releasing bends with observable pull-apart structures.

Conceptual models of pull-apart basins traditionally show a rhomboidal depression between two main parallel strike-slip faults (Figure 1a), commonly referred to as principal displacement zones (PDZs; Wu et al., 2009). This depression is bounded by oblique extensional faults termed basin sidewall faults (BSFs), linking the PDZs (Corti et al., 2020; Figure 1a).

However, the evolution and current geometry of some well-known pull-apart basins around the world cannot be fully explained by pure strike-slip motion between two PDZs (Wu et al., 2009). There is a number of pull-apart basins around the world that display distinct transtensional characteristics. For example, Umhoefer et al. (2018) note that a plate motion variation at around 8 Ma (Atwater & Stock, 1998) potentially led to successive pull-apart basin opening and flooding from south to north in the Gulf of California. Allen et al. (1997) observe that the evolution of the Bohai Basin in China can be attributed to transtension (and a later transpressional event). Armijo et al. (2002) describe submarine morphology in the Sea of Marmara that reveals a segmented fault system, including pull-apart features indicating a transtensional regime. Similarly, the Andaman Sea has been viewed traditionally as a large simple pull-apart basin but recent studies indicate that the initial orthogonal E-W or ESE-WNW extension is followed by a change in the direction of extension to SSE-WNW (e.g. Morley, 2017; Morley & Alvey, 2015; Morley & Searle, 2017; Srisuriyon & Morley, 2014). Finally, Decker (1996) and Lee and Wagreich (2017) indicate that the Vienna Basin displays similar transtensional characteristics with large negative flower structures formed over the main PDZs.

A transtensional component is sufficient to create two to three times more accommodation space for sediments compared to an orthogonal pull-apart basin (ten Brink et al., 1996). Transtensional pull-apart basins also form wider PDZs (Farangitakis et al., 2019), comprising transtensional zones ranging from elongate negative flower structures to complex zones with mini-basin characteristics themselves (Figure 1b). A transtensional pull-apart basin thus has a distinct form and evolutionary history compared with classic, purely strike-slip pull-apart basins. However, cases between these end-members can exist, where an individual basin may experience phases of both pure strike-slip and transtensional motion.

Highlights

- Analogue models test development of pull-apart basins in a transtensional rotation regime.
- Models show good correlation to the Northern Gulf of California pull-apart structure.
- First order structure also correlates well to the Bohai Basin in Northern China.
- Models highlight the need to consider rotation when investigating pull-apart basin evolution.

Understanding pull-apart basin development through analogue modelling has proven to be a very useful approach. Analogue modelling utilises materials that deform in a continuous and discontinuous manner, leading to clear expressions of the structure over time (Reber et al., 2020), which makes this method ideal for studying the evolution of a pull-apart basin. The first analogue models of pull-apart basins were carried out by McClay and Dooley (1995), who used two diverging basal plates to produce the fault geometries and surface evolution of a pull-apart basin. Similar modelling approaches have since been used by Sims et al. (1999), who studied the role of ductile decollements in pull-apart basin shape, and Smit et al. (2008), who investigated the evolution of salt diapirs in the Dead Sea pull-apart system. Withjack and Jamison (1986) explored fault patterns in oblique settings using clay models to simulate areas such as the Gulf of California and the Gulf of Aden. Basile and Brun (1999) investigated a number of parameters in pull-apart basins such as length to width ratio, brittle to ductile layer ratio, and extension velocity. Corti and Dooley (2015) and Corti et al. (2020) used centrifuge modelling apparatuses to test how the morphology of the developing pull-aparts depended on the interaction between the PDZs (underlapping, overlapping or neutral). Finally, Wu et al. (2009) used a similar array to that of McClay and Dooley (1995), imaging the development of transtensional pull-apart basins in 4D by varying the angle of the PDZ. Building on these previous studies, an in-depth investigation of the effect of changes in relative plate motion direction on pull-apart basin evolution is needed in order to understand the basin's structural response to changing boundary conditions. In this study, we use a combination of analogue modelling and seismic reflection data to further understand the evolution of pull-apart basins when transtension is imposed due to a change in extension direction during basin evolution. We then compare our model results to observations of pull-apart structures in the N. Gulf of California, where a known 10–15° change in relative plate

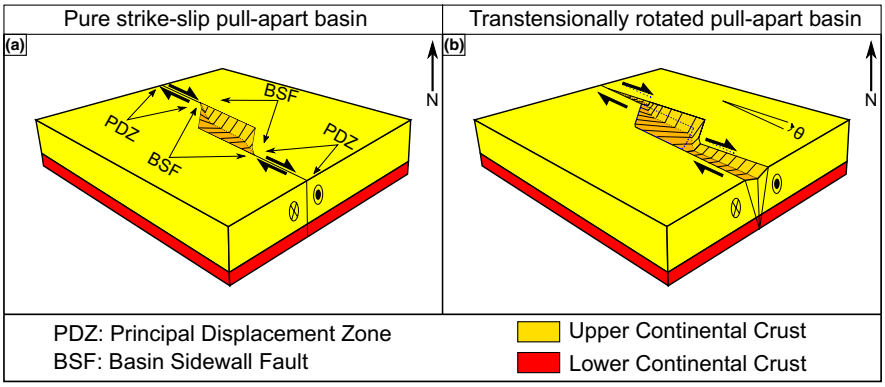

FIGURE 1 Generalised conceptual models of (a) a pure strike-slip pull-apart basin and (b) a pull-apart basin experiencing transtension (with the northern block motion rotated by $\theta = 7°$ relative to the southern block)

motion occurred at 8–6 Ma (Bennett & Oskin, 2014). Finally, we explore whether changes in extension direction during pull-apart basin evolution can explain first order features of the Bohai Basin in China. Our results show that it is important to consider changes in extension direction over time when investigating pull-apart basin evolution.

2 | GEOLOGICAL BACKGROUND

2.1 | The Northern Gulf of California

The Gulf of California (GoC) is a relatively young transtensional margin, with active seafloor spreading centres in the southern and central Gulf (Lizarralde et al., 2007) and rifting (with potential continental break-up) in the north (Martín-Barajas et al., 2013). All the extensional components of the GoC (spreading centres and rifts) are connected through dextral transform faults (Figure 2d). The first occurrence of dextral transform motion between the Pacific and North American plates is believed to have happened ca. 20 Ma (Atwater & Stock, 1998; Axen, 1995; Bennett et al., 2013; Lonsdale, 1989; Figure 2a), followed by the first phase of extension in the Proto-Gulf of California starting ca. 12 Ma (Atwater & Stock, 1998; Stock & Hodges, 1989; Figure 2b). Bennett and Oskin (2014) suggest that a ~10–15° clockwise rotation in the relative motion between the plates between 12.5 and 6.5 Ma increased the rift obliquity and favoured the development of strike-slip faulting. Shearing localised in en-echelon strike-slip shear zones, that began to create pull-apart basins by 6 Ma (Bennett et al., 2013; Figure 2c). These nascent pull-apart basins flooded from south to north successively due to higher transtensional deformation rates further from the Euler pole (Umhoefer et al., 2018). At the end of their evolution, and after a further plate re-organisation at ca. 3 Ma (Seiler et al., 2009), a series of long dextral transform faults was formed, connected by smaller rift basins (Lizarralde et al., 2007; Persaud et al., 2003; Figure 2d). In the northern GoC, the nature and timing of continental break-up is still unclear, with the presence of oceanic crust suggested in some basins (González-Escobar et al., 2014; Martín-Barajas et al., 2013) and delayed rupture suggested for others (Lizarralde et al., 2007; Martin-Barajas et al., 2013).

Deformation in the northern GoC is distributed across a broad, relatively shallow depression representing a pull-apart structure between the Cerro Prieto Fault (CPF) and the Ballenas Transform Fault Zone (BTFZ; Persaud et al., 2017; Figure 2e). Within this pull-apart structure, a dense network of mainly oblique-normal, small-offset faults forms a broad zone of brittle deformation, with smaller sub-parallel basins along splays at the NW end of the Ballenas Transform Fault Zone (Persaud et al., 2003; Figure 2e). Hence, the basal ductile shear zone underneath the brittle crust is expected to be as wide as the surface deformation (Persaud et al., 2003). Deformation within the pull-apart structure has experienced a westward jump from the Tiburon Basin ca. 3.5–2 Ma following a plate reorganisation (Lonsdale, 1989; Seiler et al., 2009). The Ballenas Transform Fault Zone and Cerro Prieto Fault have a 10° difference in strike, with earthquake and field data suggesting that between 7–15 mm/a of dextral slip is transferred from the northern end of the Ballenas Transform Fault Zone to the onshore faults in Baja California (e.g. Bennett et al., 1996; Goff et al., 1987; Humphreys & Weldon, 1991). Moreover, the Cerro Prieto Fault and Ballenas Transform Fault Zone strike 6–7° clockwise (312°) of the transforms in the south (305°; Lonsdale, 1989). Dorsey and Umhoefer (2012) and Van Wijk et al. (2017) argue that this increased obliquity, in combination with the geometry of the strike-slip faulting stepover, contributes to the northern Gulf's basin development and late or absent rupture. Other factors that contribute to the northern Gulf's development could include initial fault geometries, thick sedimentation, and changing loci of extension.

2.2 | The Bohai Basin, Northern China

The Bohai Basin in Northern China is a 1,000 km long by 600 km wide extensional structure, formed mainly in the early Cenozoic (Hu et al., 2001; Liangjie et al., 2008), which has undergone a transtensional phase in its evolution (Allen et al., 1998). It has a NE-SW trend, bounded

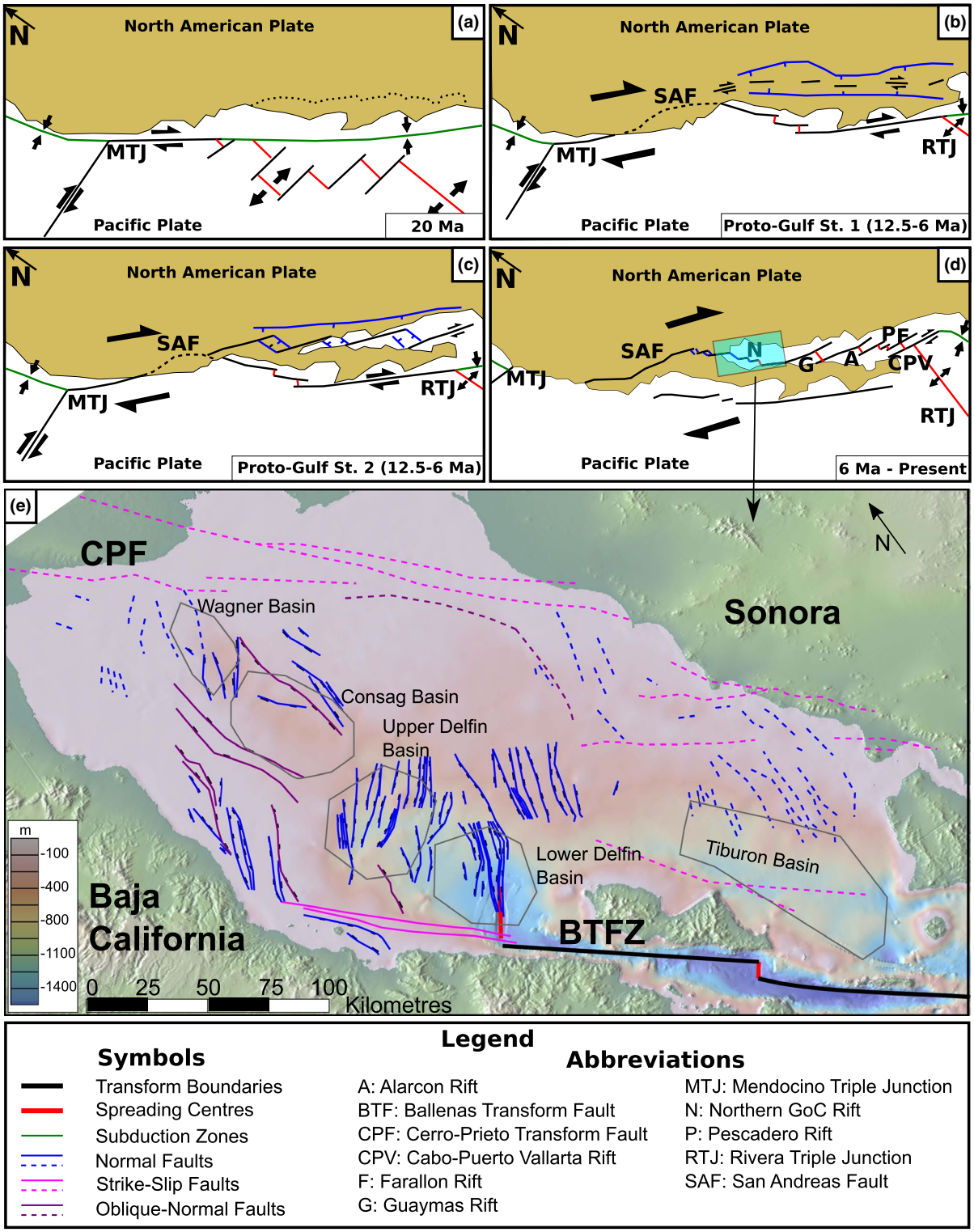

FIGURE 2 (a-d) Stages of evolution of the Gulf of California from 20 Ma to present (modified from Bennett et al., 2013), (a) Initial occurrence of dextral transform motion, (b) early extension in the proto-gulf, followed by (c) transtension in the proto-gulf, (d) current configuration. (e): close-up map of the northern Gulf of California (faults in continuous lines from this work and Persaud et al., 2003, faults in dashed lines from Martín-Barajas et al., 2013, basins outlined in grey)

by lithospheric scale strike-slip faults, namely the dextral Tan-Lu strike-slip fault zone in the east (Allen et al., 1997; Klimetz, 1983) and the Lanliao and Shulu-Handan strike-slip fault zones in the west (Qi & Yang, 2010; Figure 3c). It superficially resembles a giant pull-apart structure, controlled by dextral slip, with the Bozhong Depression (Figure 3a) being the main Cenozoic depocentre. Transtension in the basin occurred in the Early Cenozoic

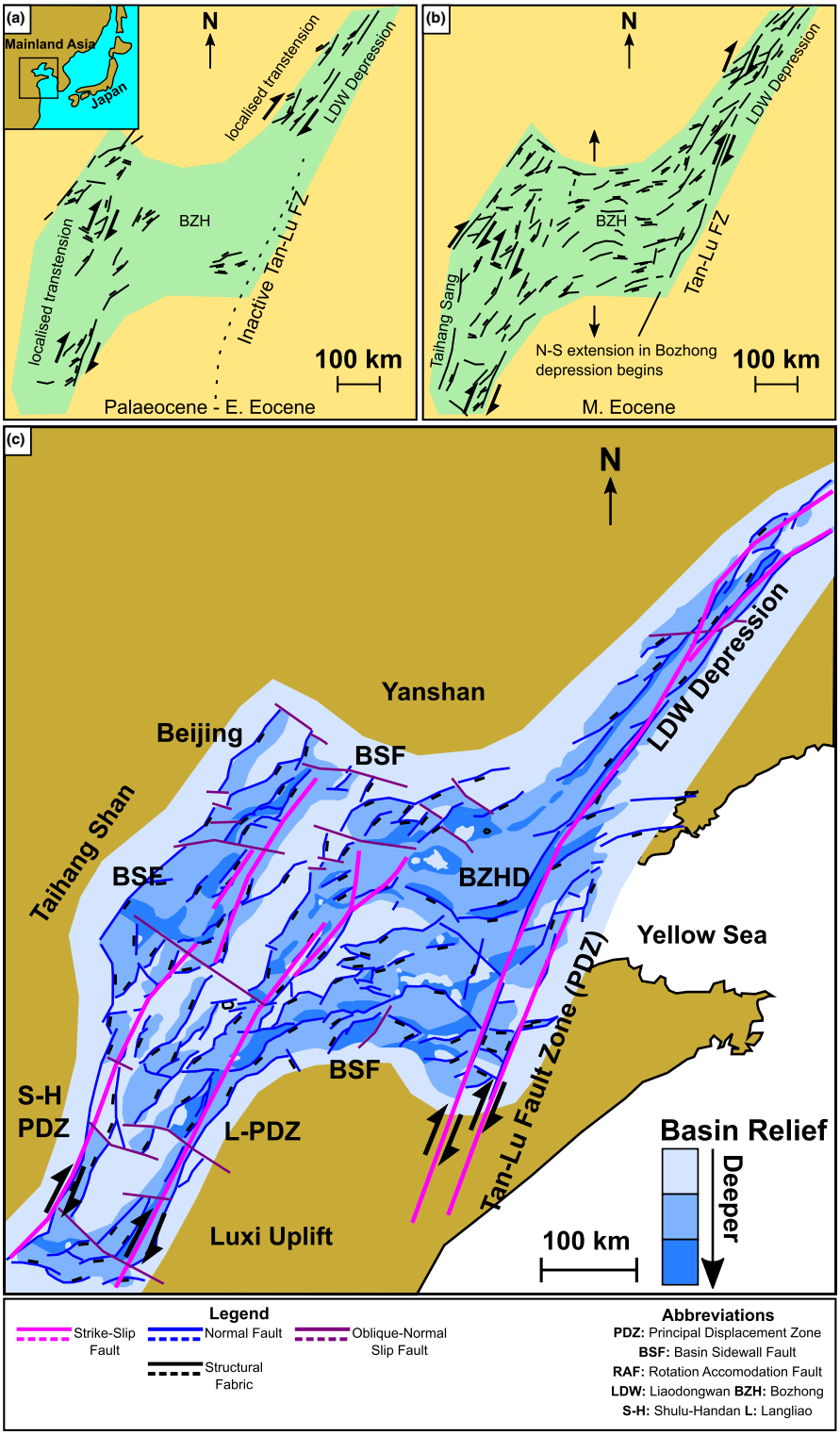

FIGURE 3 (a-b) Evolution of the structural fabric of the Bohai Basin (modified from Allen et al., 1997). Location of the basin shown in pale green. Inset: regional location of panels (a-c). (c) Map of the structure and relative depth to Mesozoic basement and structural map of the Bohai Basin (modified from Allen et al., 1997 and Qi & Yang, 2010). Note that panels (a-b) refer only to the structural fabric of the area. BZHD: Bozhong Depression. The colours in the legend refer only to panel (c)

when the Pacific-Asia convergence vector rotated from NW-SE to E-W (Engebretson et al., 1985).

Results from different approaches such as seismic reflection (Feng & Ye, 2018; Qi & Yang, 2010), stress field modelling (Guo et al., 2009), thermal subsidence (Hu et al., 2001) and hydrocarbon well data (Liangjie et al., 2008) suggest that the Bohai Basin has had a multi-phase evolution. The basement fabric of the Bohai Basin is of pre-Cenozoic age, and consists of Precambrian to Mesozoic metamorphic and sedimentary rocks that are cross-cut by the main boundary faults of the basin (Qi & Yang, 2010). In the Paleocene to Early Eocene, dextral transtension was localised in four regions in the basin, which acted as the main depocentres at the time (Allen et al., 1997; Figure 3a). By the Middle Eocene, extension had propagated southwards from the current location of the Liaodongwan Depression, creating extensional overlap

over the main depocentre of the central basin, the Bozhong Depression (BZHD Figure 3b). Extension along east-west normal faults in this region led to the thickest known sediments in the basin (Allen et al., 1997; Qi & Yang, 2010).

3 | METHODOLOGY

3.1 | Analogue Models

3.1.1 | General parameters of the models

We use a modified experimental apparatus based on Farangitakis et al. (2019; originally inspired by Basile & Brun, 1999), where a moving plate slides away from a static plastic sheet at the base of a brittle/ductile layer configuration (Figure 4a). Hence, deformation is entirely driven through the applied basal boundary conditions, with pre-imposed velocity discontinuities (VDs), similar to those in Allemand and Brun (1991) and Tron and Brun (1991). The velocity discontinuity configuration is that of an en-echelon rift and strike-slip system, consisting of two sets of alternating discontinuities parallel and perpendicular to orthogonal plate motion (Figure 4a). The master strike-slip faults or PDZs are "neutral" (Corti & Dooley, 2015; Corti et al., 2020), meaning they do not overlap or underlap each other during orthogonal motion.

Following an initial orthogonal extension phase, we introduce a counterclockwise rotation of 7° in the extension direction, consistent with half the amount of rotation observed in the northern Gulf of California (10–15°—Bennett & Oskin, 2014). We use 7° of rotation mainly due to physical limits of the apparatus.

The brittle/ductile experiments were performed with the basal plate moving with a velocity of 7.5 cm/h, a velocity scaled to the natural example (see model scaling section). We capture the evolution of the model's surface features using a high-resolution digital camera taking snapshots every 60 s (with a resolution higher than 1 cm). This allows for a time-based analysis of the developing surface features after the model run. We also map the changing topography using a 3D surface scanner (with accuracy >1 mm) that scanned the model surface every 3 min. This technique enables us to (a) quantify topographical changes in the model and (b) identify structural features that have developed and might not be visible in the top-view images. Finally, at regular intervals (of ~2.5 min) we use a small funnel to manually add three alternating colour layers of feldspar sand in the topographic lows. These layers represent syn-and post-rift sedimentation and are particularly useful in correlating structures and identifying the locus of extension when the models are sectioned and reconstructed in 3D. At the end of the experimental run, the model is also covered with a thick protective layer of black sand prior to wetting and cutting.

3.1.2 | Kinematic set-up of the analogue models

The model configuration (Figure 4) allows us to investigate the effects of transtensional rotation on a pull-apart basin developing between two strike-slip velocity discontinuities (Basile & Brun, 1999). The rotating plate is represented by a 46 × 21 cm plastic plate underneath the silicone putty/feldspar sand layers. The shape of the moving plate (as seen in Figure 4a) imposes two right-lateral strike-slip faults connected by a rift segment. At the trailing edge of the plate, a thin plastic sheet is fixed above the moving plate to act as a second velocity discontinuity, imposing another rift (Figure 4a). The plate is guided by a series of metal bars at its front and trailing ends. These ensure that (a) movement initially remains almost orthogonal and (b) rotation at the later stage is not greater than 7° (Figure 4a, grey boxes labelled guide bars). Once motion starts, the plate moves almost orthogonally, creating a pull-apart structure between the ends of the two strike-slip faults and a further rift at the back end (Figure 4b). A construction of heavy metal blocks, welded firmly on the table top, acts as a mechanical elbow (Figure 4a, yellow boxes). When the plate reaches the two boxes, which are placed at an angle, it is forced to rotate until it leaves the top end of the elbow, simultaneously hitting the top left guide bar. The top left guide bar stops any further rotation and ensures the plate has a consistent new vector of motion. (Figure 4c). In this rotation stage, the previously formed structures undergo rotation-dominated transtension and oblique rifting (Figure 4c). Finally, after rotation has ended, the plate slides between the top guide bars, moving with the new plate motion vector, oblique to the original boundary (Figure 4d). The model is extended for a total of 7 cm.

3.1.3 | Model rheology, materials and scaling

Continental crust in our models is represented as follows (Figure 5 and Table 1):

a. For the brittle upper crust, we use a 1.6 cm thick layer of dry feldspar sand (deformable according to the Mohr-Coulomb criterion) with a density of ρ = 1.3 g/cm^3 (Luth et al., 2010; Sokoutis et al., 2005; Willingshofer et al., 2005), an internal friction coefficient of μ_{fric} of 0.6 (Willingshofer et al., 2018), and sieved to a grain size d = 100–350 μm. The sand is sieved evenly over the model during the modelling set-up stage.
b. Ductile lower crust is modelled with 0.8 cm thick layer of transparent silicone putty SGM-36, a poly-dimethyl siloxane with a density of ρ = 0.970 g/cm^3, no yield strength and viscosity at room temperature of μ_{vis} = 5×10^4 Pa s (Weijermars, 1986a; Weijermars, 1986b; Weijermars 1986c).

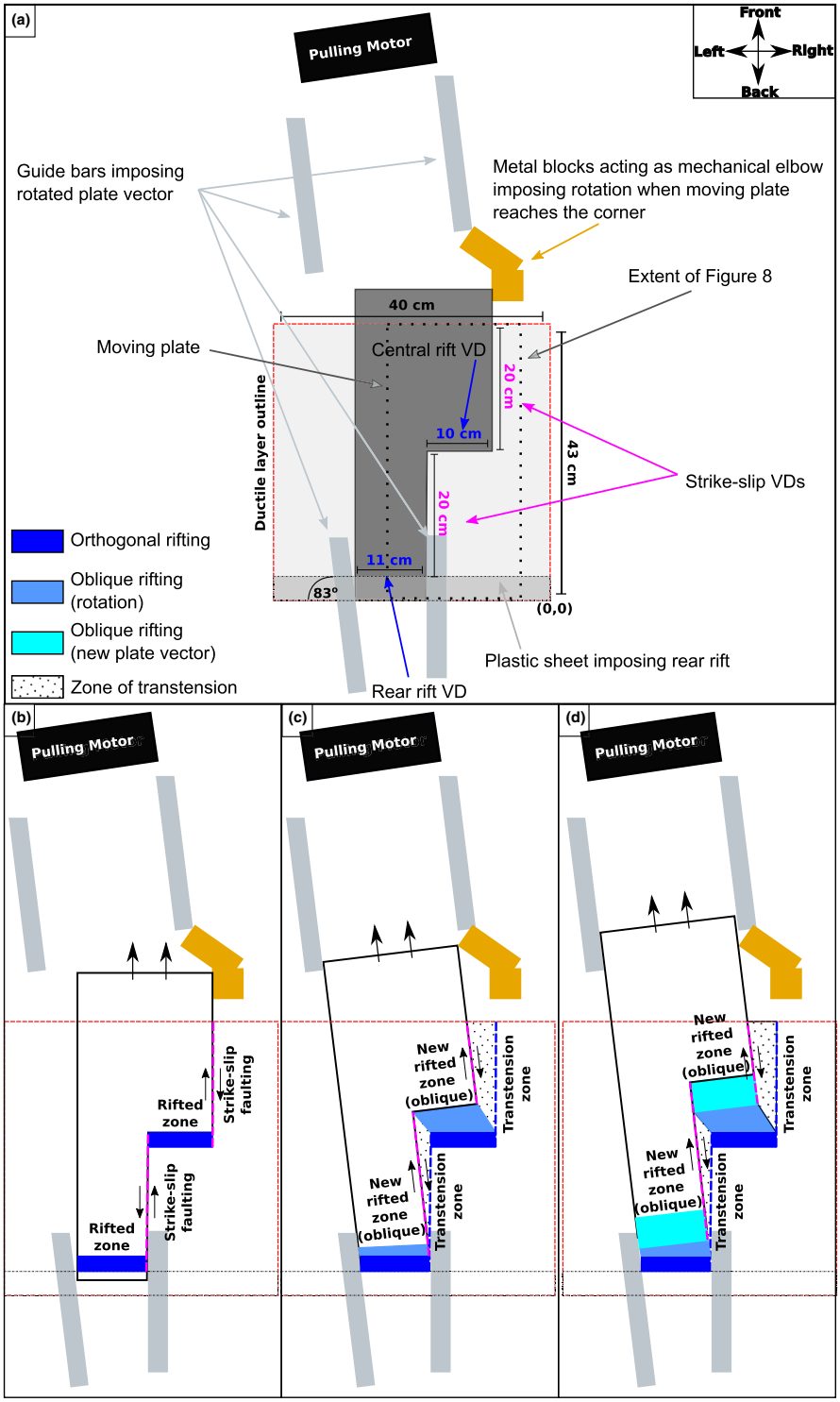

FIGURE 4 Model apparatus: (a) parts, dimensions, and initial configuration of the model apparatus (b) orthogonal motion stage, (c) end of rotation stage, (d) new oblique plate motion vector stage. Red box marks the model boundary, dark grey box marks the moving plate. Yellow boxes represent the mechanical elbow that imposes the rotation. Elongate darker shaded grey area in the back of panel a marks the fixed plastic sheet acting as the second rift

The selection of the model layer materials is based on feldspar (or quartz) sand being the most common material used to represent the upper brittle crust while PDMS silicones are a very good analogue for ductile layers (Reber et al., 2020).

The governing equations for the layer strength are derived from Brun (2002). In the brittle layers, the strength profile along the strike-slip faults is given by the equation:

$$\sigma 1 - \sigma 3_{(ss)} = \rho_b g z_b \tag{1}$$

where $\sigma 1 - \sigma 3_{(ss)}$ is the brittle layer strength along the strike-slip faults, ρ_b is the brittle layer density, g is gravitational acceleration and z_b is thickness of the sand layer (Brun, 2002).

For extension in the brittle layers, the governing equation is:

$$\sigma 1 - \sigma 3_{(r)} = \frac{2}{3}(\sigma 1 - \sigma 3)_{(ss)} \quad (2)$$

where $\sigma 1 - \sigma 3_{(r)}$ is the extending brittle layer's strength (Brun, 2002).

For the ductile layer, the strength is:

$$\sigma 1 - \sigma 3_{(d)} = 2\left(\eta \frac{V}{z_d}\right) \quad (3)$$

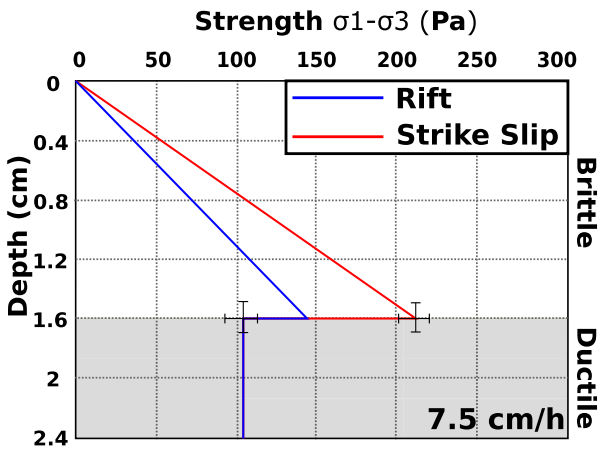

FIGURE 5 Model strength profile. White background: brittle layer, grey background: ductile layer]

where $\sigma 1 - \sigma 3_{(d)}$ is ductile layer strength, η is ductile layer viscosity, V is the velocity of the moving plate and z_d is ductile layer thickness (Brun, 2002).

These equations produce a rheological profile as shown in Figure 5. This strength profile is applicable only to the very early stages of deformation in our model, in particular, before significant changes in thickness occur.

We scale our analogue models to their natural prototype based on the principle of maintaining similarity in the structural geometry, the kinematics and the rheology of the crust (Hubbert, 1937; Ramberg, 1981; Weijermars & Schmeling, 1986; Sokoutis et al., 2000; Sokoutis et al., 2005). For the initial crustal thickness, we used an average value of 37.6 km (Persaud et al., 2007, 2015). In our 2.4 cm thick model this translates to a model to nature length scale ratio of 6.4×10^{-7}.

We achieve rheologic and dynamic similarity in our models by scaling the gravitational stress, σ (Dombradi et al., 2010):

$$\sigma^{\propto} = \rho^{\propto} g^{\propto} z^{\propto} \quad (4)$$

where ρ is density, g is gravitational acceleration, z is thickness and the "$\propto$" symbols denote the model to nature ratio (Sokoutis et al., 2005). For the viscous deformation, the ratio between

TABLE 1 Materials and parameters used in the models for scaling to nature

Materials	Parameters (SI units)	Model	Nature	Model/ nature ratio
Brittle upper crust (K-Feldspar sand)	Thickness (m)	1.60×10^{-2}	2.51×10^{4}[a]	6.4×10^{-7}*
	Density (kg/m^3)	1.30×10^{3}[b,c,d]	2.70×10^{3}[e]	0.48
	Internal friction coefficient	0.60[f]	0.80[g]	0.80
	Cohesion (Pa)	15[h]	2.00×10^{6}[i]	7.50×10^{-6}
	Strength (Pa)	2.04×10^{2}	5.00×10^{8}[e]	4.00×10^{-7}
Ductile lower crust (silicone polymer)	Thickness (m)	0.8×10^{-2}	1.25×10^{4}[a]	6.4×10^{-7}*
	Density (kg/m^3)	0.97×10^{3}[j,k,l]	2.90×10^{3}[e]	0.33
	Viscosity (Pa s)	5×10^{4}[j,k,l]	10^{22}[m]	5×10^{-18}
	Strength (Pa)	104	4.40×10^{7}[a]	2.4×10^{-6}
General parameters (SI units)				
Extension velocity (m/s)		2.08×10^{-5}	7.3×10^{-10}[n]	2.9×10^{4}
Strain rate		2.6×10^{-3}	5.9×10^{-14}	4.5×10^{10}
Time (s)		4.02×10^{3}	1.89×10^{14}[n]	2.12×10^{-11}
Length of pull-apart basin (m)		0.31	2.00×10^{5}	1.60×10^{-6}
Width of pull-apart basin (m)		0.15	10.00[5]	1.50×10^{-6}
L/W ratio of pull-apart basin		2.1	2.00	1.05
Smoluchowski number		0.94	1.2	0.79
Ramberg number		0.59	0.61	0.95
Reynolds number		3.38×10^{-8}	2.92×10^{-23}	N/A

Note: For calculation of parameters refer to main text (Values obtained from a: Persaud et al., 2015; b: Sokoutis et al., 2005; c: Willingshofer et al., 2005; d: Luth et al., 2010; e: Burov, 2011; f: Willingshofer et al., 2018; g: Brace & Kohlstedt, 1980; h: Dombradi et al., 2010; i: Farangitakis et al., 2020; j: Weijermars, 1986a; k: Weijermars, 1986b; l: Weijermars, 1986c; m: Persaud et al., 2017; n: Brune et al., 2016).

*Ratio calculated for the combined thickness of brittle and ductile crust.

gravitational and viscous stresses is given by the Ramberg Number (R_m – Weijermars & Schmeling, 1986):

$$R_m = \frac{\rho_d g z_d}{\eta \dot{\varepsilon}} \tag{5}$$

where ρ_d is the ductile layer density and $\dot{\varepsilon}$ is the strain rate.

To scale brittle deformation, we used the ratio between gravitational stress and cohesive strength, the Smoluchowski number (S_m – Ramberg, 1981):

$$S_m = \frac{\rho_b g z_b}{\tau_c + \mu_c \rho_b z_b} \tag{6}$$

where τ_c is the cohesive strength and μ_c is the internal friction coefficient. For accurate scaling, the individual R_m and S_m values of models and natural prototypes should be as similar as possible (with the ideal value being a ratio of 1:1; Dombradi et al., 2010). For our model, these model/nature R_m and S_m ratios are 0.95 and 0.79 (Table 1). As previous work suggests, if the Reynolds number (Re) is relatively low, then inertial forces can be neglected compared to viscous ones (Del Ventisette et al., 2007; Dombradi et al., 2010; Wickham, 2007). The Reynolds number is given by:

$$Re = \frac{\rho V l}{\eta} \tag{7}$$

where V is the velocity of the moving plate and l is the total extension length. The N. GoC has a relative plate velocity of 23 mm/a from 12–6 Ma and 50 mm/a onwards (Brune et al., 2016), and our model extends at 7.5 cm/hr (Table 1). Thus, we can estimate the extension length in both cases, resulting in low Reynolds numbers for model and nature (3.38×10^{-8} and 2.92×10^{-23} respectively). This allows the scaling of different forces to deviate from strict dynamic similarity, so the time and length ratios can be considered independent variables (Ramberg, 1981).

3.1.4 | Digitising the analogue models

After the model run, the model is wetted with a mixture of water and soap and left overnight for the liquid to permeate through the brittle layer. We then proceed to cut the model in 12 equidistant cross-sections (every 4 cm). These are cut at an angle of 70° to the orthogonal pulling direction, to capture as many of the emergent oblique structures as possible in each cross-section. Before the start of the experiment, graticules are drawn on the modelling surface to act as control points for georeferencing the top-view images taken during the model run and for locating the cross-sections. All of the top-view images are stacked in ArcGIS and georeferenced using these graticule points. A Cartesian coordinate system is assigned with point 0,0 being the bottom right corner of the model (as marked in Figure 4a). We then extract the exact coordinates of each cross-section in the form of a polyline feature. Photographs of the cross-sections are processed in Adobe Lightroom™, including lens and distortion corrections. Subsequently, the cross-sections are redrawn as vector graphics and inserted into the seismic interpretation software Schlumberger Petrel™, where they are projected into 3D space (Figure 6a). We then interpret the interface between each different coloured sand layer as a horizon. Using the interpreted horizons, we produce a solid block model from the cross-sections, populating the space between each cross-section by interpolating linearly between the horizon points (Figure 6b).

3.1.5 | Analogue modelling limitations

First, in this work we carry out a single specific experiment designed to replicate the evolution of the Gulf of California. However, it can be applied to other examples around the world with similar structure (as seen in Reber et al., 2020), and we extend our study with a comparison to the Bohai Basin. For a parametric study on the effects of transtension and transpression on strike-slip boundaries with a similar apparatus, we refer readers to Farangitakis et al. (2019). Relative motion between the basal plates varies during the first cm of deformation and deviates from purely orthogonal by ~0.5° due to experimental conditions. Nonetheless, this early deformation remains within the range whereby natural examples would still be classified as orthogonal. Second, since our models represent only the continental crust, we operate under the assumption that the mantle underneath accommodates a similar plate motion. Finally, our physical analogue model does not include erosion, isostatic compensation or heat transfer between the layers.

3.2 | Seismic reflection data

We use the UL9905 high resolution reflection 2D seismic dataset acquired by LDEO, Caltech, and CICESE (Stock et al., 2005), which is publicly available for download at the URL: http://get.iedadata.org/doi/303736. The data were acquired with a 48 channel, 600 m streamer, at a sampling interval of 1 ms (shot spacing of 12.5 for Lines 2–52 and 25 m for Lines 53–80) and were recorded for 2–3 s. (Stock et al., 2005). The spatial coverage of the data is presented in Figure 7. The seismic interpretation is based on Persaud et al. (2003) and

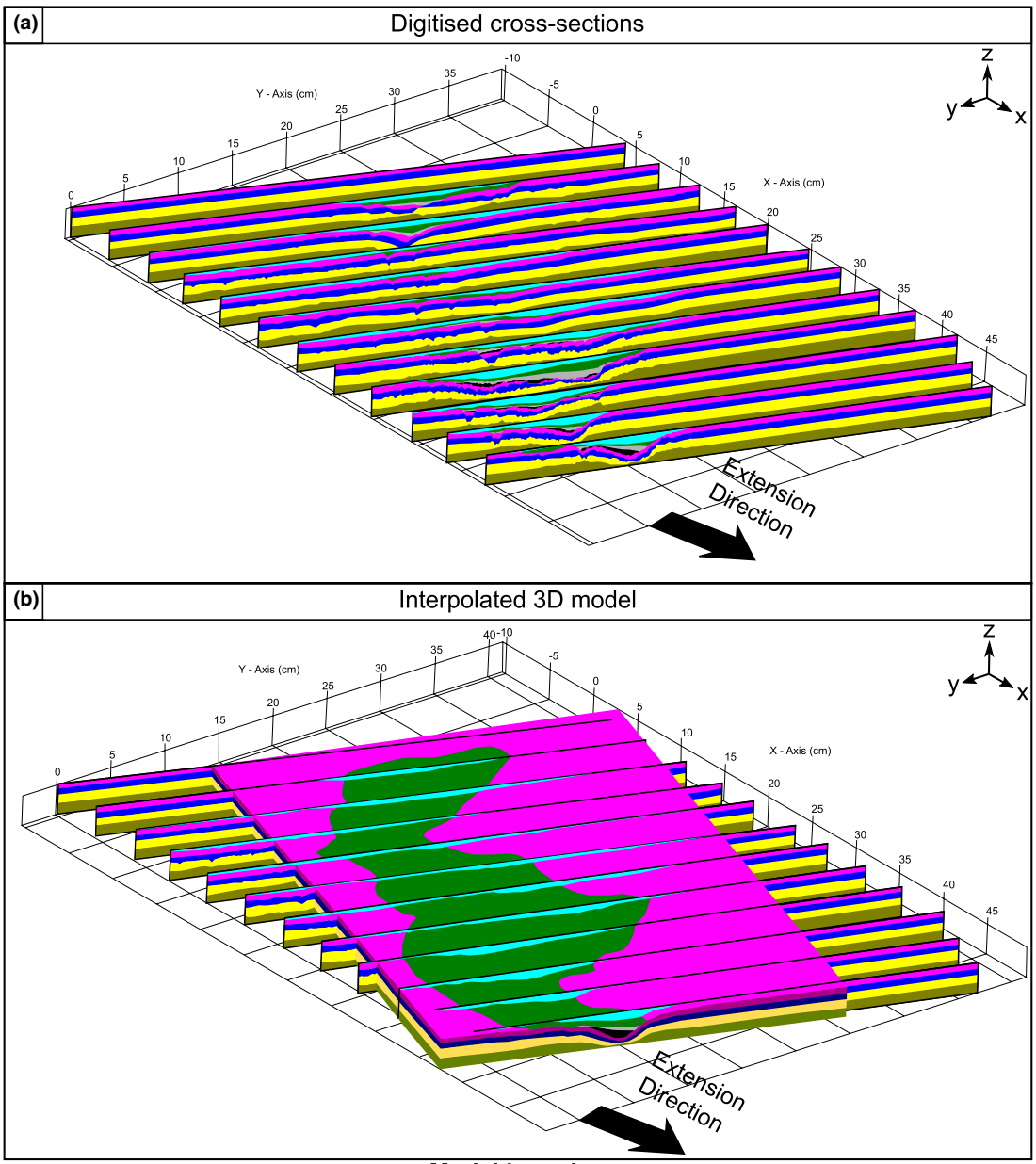

Model Layering

Original Layer Colour	Digitised Layer Colour	Description	Role of Layer
Black	Cyan	Quartz sand	Protective cover (added)
Green	Green	Feldspar sand	Post-rotational sediments (added)
White Black	Gray Black	Feldspar sand	Syn-rotational sediments (added)
Pink Blue Yellow	Pink Blue Yellow	Feldspar sand	Brittle upper crust (original)
Transparent	Brown	Silicone putty	Ductile lower crust (original)

FIGURE 6 Digitised analogue model: (a) Digitised model cross-sections, (b) solid block 3D model. Note the changes in colour between the experiment and the digitized model for interpretation purposes. To better show the geometry of the pull-apart, the lateral extent of the protective layer (cyan colour) is not shown. For an enlarged version of panels (a and b), refer to Figures S1 and S2

Martín-Barajas et al. (2013) combined with new observations in 3D. For the 3D interpretation, faults were correlated based on their throw across adjacent seismic profiles. The main visible seismic horizons are picked and correlated to their mappable extent by tying observations between seismic cross-sections. Since there are no publicly available well data, the age correlation between the picked seismic horizons is based on well-tie constrained interpretations of Martín-Barajas et al. (2013).

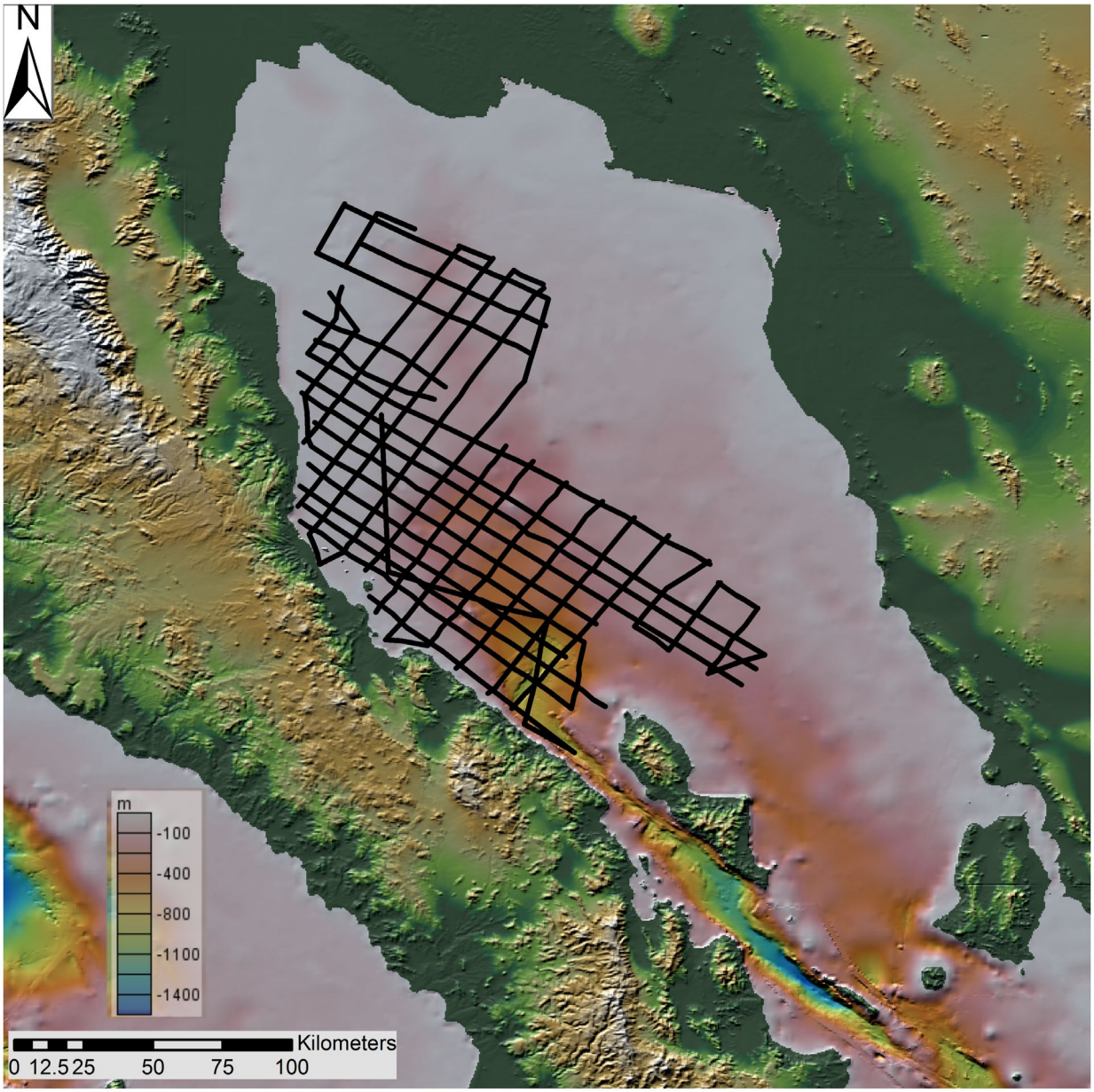

FIGURE 7 Location of the UL9905 high-resolution reflection seismic dataset (black lines; Stock et al., 2005). Bathymetry and topography from GMRT Grid Version 3.3 (Ryan et al., 2009)

Finally, the sense of slip on faults is inferred for certain faults (such as the basin sidewall faults) from interpretations from pre-existing literature and after comparison with the analogue models (e.g. for faults that evolve from purely normal to oblique-normal). For the Bohai Basin, we use seismic data taken from Qi and Yang (2010).

4 | RESULTS

We describe the surface fault evolution, timing and kinematics of the model based on our observations of the model top-view photographs and cross-sections. We use the surface scanner-derived topography to identify normal faults and the pink marker lines to identify strike-slip motion (Figure 8). If a fault scarp displays both a change in topography and a horizontal displacement of marker lines, it is termed an oblique-normal structure.

4.1 | Orthogonal stage

After about 0.7 cm of orthogonal motion of the moving plate, the first surface indications of strike-slip deformation on the

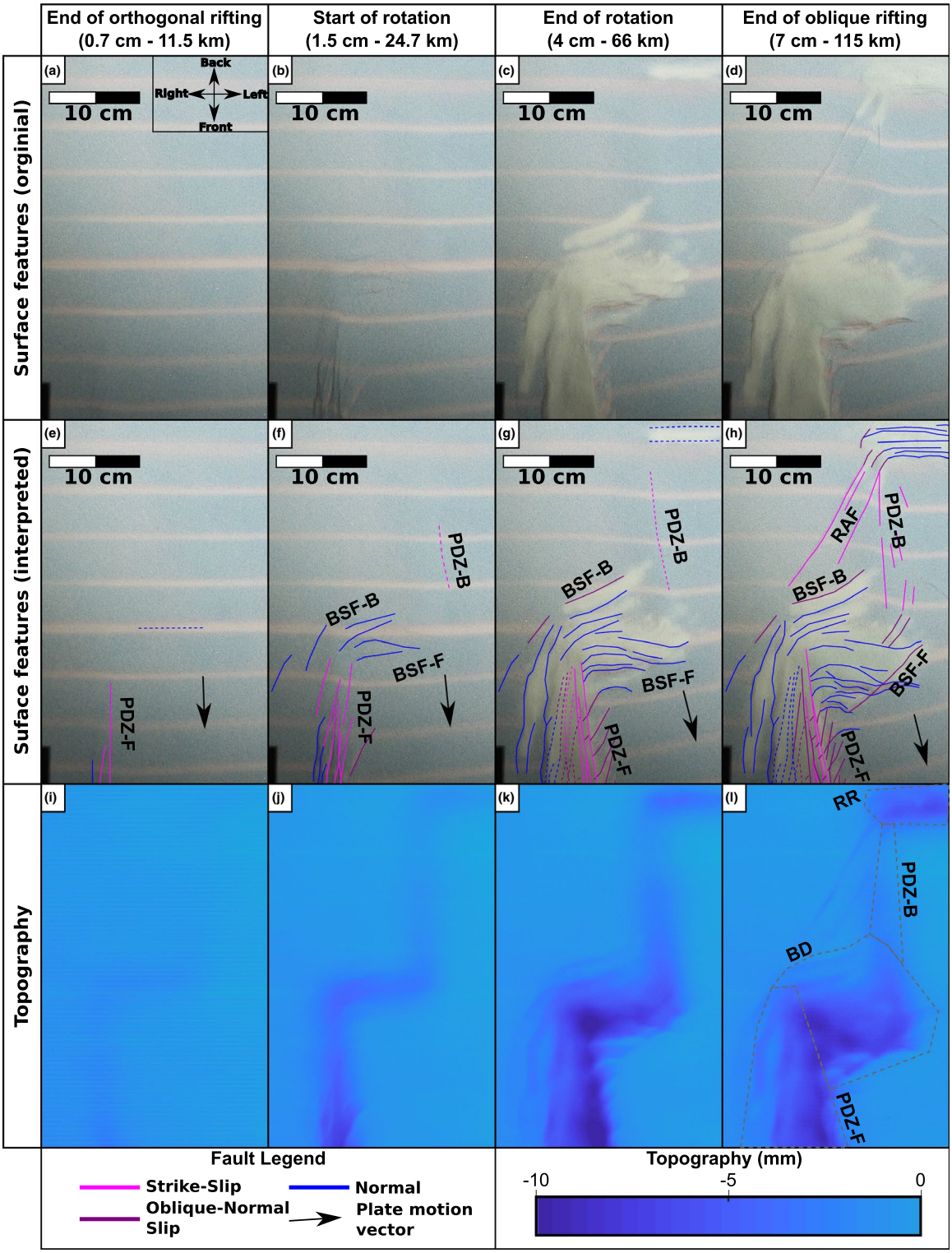

FIGURE 8 Analogue modelling experiment results. (a–d) Surface feature development. (e–h) Surface feature development (interpreted), showing the development of normal, oblique and strike-slip faulting. (i-l) Topography evolution. PDZ-F/B: Principal Displacement Zone (Front/Back), BSF-F/B: Basin Sidewall Fault (Front/Back), RAF: Rotation Accommodation Fault, BD: Basinal Depression, RR: Rear Rift. The terms Front/Back are defined in panel a. The PDZs and MBA are outlined in panel l of this Figure. Figure outline labelled in Figure 4. For larger versions of the panels, refer to Figures S3-S14

PDZ appear as dextral displacement of the pink marker lines in a ~10 cm long region of the front end of the moving plate (Figure 8e, PDZ-F). The basinal depression begins to form in the middle of the moving plate as a subtle orthogonal depression feature in the surface scanner topography depiction (Figure 8i, center).

4.2 | Rotation stage

Start of rotation: After about 1.5 cm of movement, the basal plate reaches the mechanical elbow that imposes rotation. At that stage, the PDZ is about 5 cm wide, and is composed of multiple strike-slip segments, while the fixed side of the model displays components of normal displacement. Over the front edge of the moving plate, oblique-normal faults begin to appear at an angle between 15–30° to the plate vector, resembling P shears (Tchalenko, 1970; Figure 8f, PDZ-F). The basinal depression is more pronounced with higher topographic relief (~4–5 mm – Figure 8j, centre). The first basin sidewall faults start to develop (Figure 8f, middle), defining the basinal depression zone, which is 5 cm wide. The second PDZ can be seen through the slight displacement of the pink marker lines (Figure 8f, PDZ-B).

End of rotation: After another 2.5 cm of movement (4 cm in total), the PDZ has developed into a triangular-shaped transtensional zone almost 10 cm wide, with the main strike-slip motion migrating with the moving plate boundary. On the fixed side of the experiment, normal faults develop to accommodate the extensional component of transtensional shear (Figure 8g, PDZ-F). A series of oblique-normal faults developed along the whole length of the front PDZ in the part of the moving plate. The pull-apart depression is now well developed with elongate basin sidewall faults, which are oriented to accommodate transtensional rotation (Figure 8g, centre and Figure 8k). The main depression reaches a minimum elevation of about a 1cm below the original horizontal level to the top of the added sediments) and is about 12 cm wide (Figure 8k). From the displacement of the pink marker lines along the rear basin sidewall fault, we can infer an oblique-normal faulting character (Figure 8g, BSF-B). At the rear end of the plate, the second rift starts to develop as a narrow graben, ~2.5 cm wide (Figure 8g, top and Figure 8k, top – area labelled RR in Figure 8l).

4.3 | Final plate vector stage

At this stage, the moving plate has acquired its final motion vector (Figure 8h). After a further 3 cm of motion, the front PDZ is well developed, with pure strike-slip motion occurring over a narrow zone visible in the surface evolution (Figure 8h, PDZ-F) and in the topography (Figure 8l, bottom). The PDZ at the rear end of the plate is now visible on the surface with two longer and a few shorter strike-slip fault segments (Figure 8h, PDZ-B). The basin sidewall faults on the trailing side of the plate are further developed (Figure 8h, BSF-B), while on the frontal edge, a new major oblique-normal fault has developed in response to the new motion vector, cross-cutting the previous basin sidewall faults (Figure 8h, BSF-F). The angle of this new oblique-normal fault is ~50° to the previous normal faults and almost perpendicular to the new motion vector (80°). The second oblique rift at the back end of the plate (Figure 8l, RR) is now fully developed with curved oblique-normal faults on its flank. Finally, two strike-slip faults form oblique to the plate motion and appear to accommodate the rotation of the rear PDZ system (RAF in Figure 8h). We term these faults rotation accommodation faults (RAFs).

It is worth noting that while the model extends for 7 cm in the orthogonal sense, factoring in the extension velocity of 7.5 cm/hr and the model runtime (65 min), the total extension should amount to 8.4 cm. However, 16% of the total extension is accommodated through the rotational motion through oblique-normal faulting. Scaling to the natural example would result in ~115 km of orthogonal extension and 138 km of total extension.

5 | DISCUSSION

5.1 | Comparison with the N. Gulf of California (N. GoC) pull-apart

We compare faulting and sedimentation patterns from the high resolution UL9905 seismic dataset (Stock et al., 2005) in the N. GoC to those in our model. The N. GoC is thought to have undergone a change in the relative plate motion vector at 8 Ma (Atwater & Stock, 1998) and a plate boundary jump ca. 3 Ma (Lonsdale, 1989), giving it its current morphology. This plate boundary jump resulted in the abandonment of the basins in the eastern N. GoC. In our model, we can replicate the rotation that led to the formation of the pull-apart basin, but not the plate boundary jump. Therefore, we focus our observations on the effect the rotation has had on the broader N. GoC structure and, by comparison with our model, infer that the rotation set the initial structural framework for the current GoC. For the seismic interpretation of stratigraphic horizons, we interpreted the most prominent reflectors that were cross-correlatable across the 2D seismic line network and determined their relative age using inferred ages of seismic stratigraphy in the region (Martín-Barajas et al., 2013).

5.1.1 | Fault evolution

We observe similar first-order evolution patterns between our experiment and the Northern Gulf of California both in map and 3D view (Figure 9).

Examining the structures in map view, we observe that in both our experiment and in the N. GoC, the basins are bounded by oblique-normal slip faults (labelled as BSFs in Figure 9). In the north of the Gulf, these are the faults branching at a 60–90° angle from the northern end of the

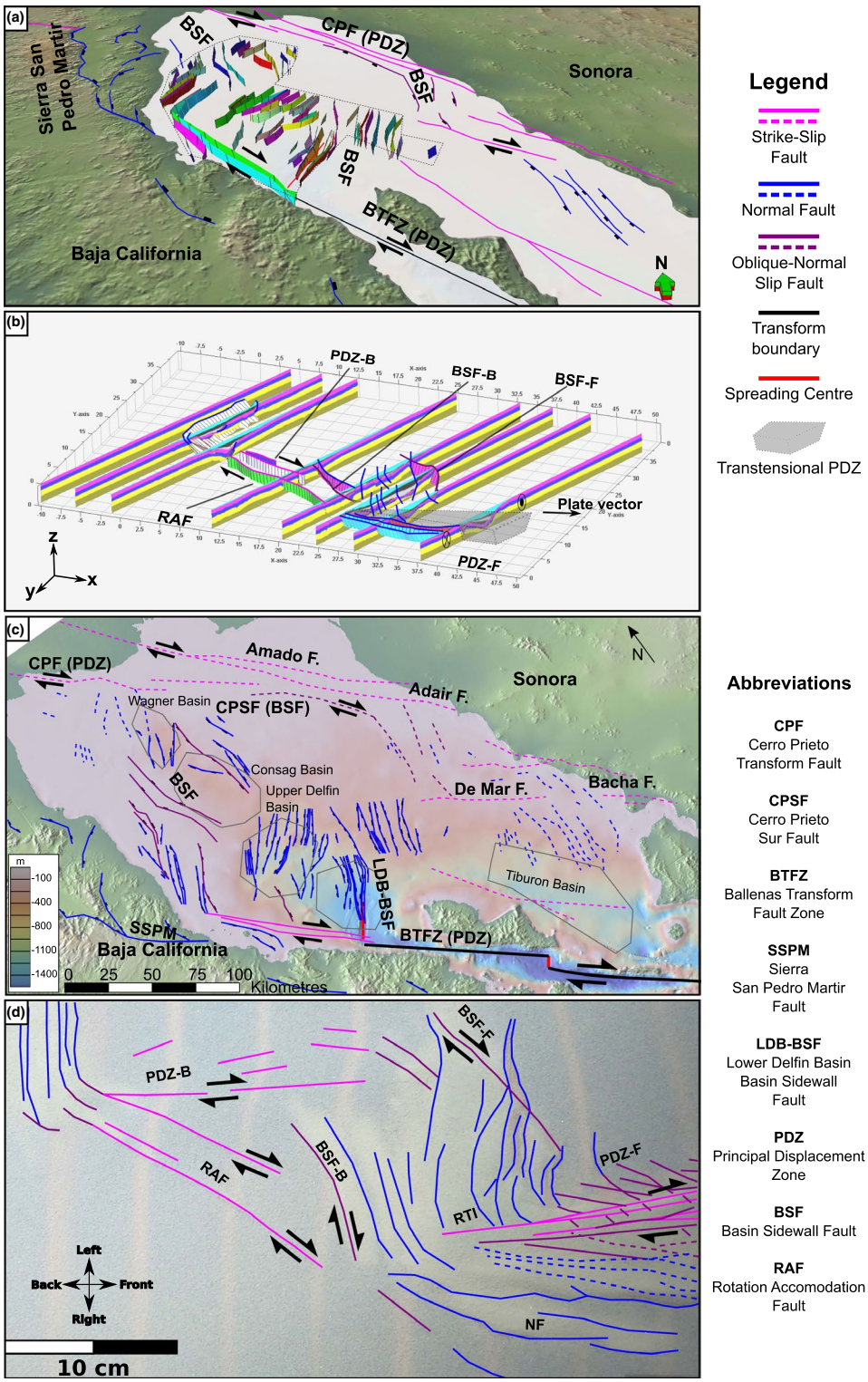

FIGURE 9 Comparison between our model and faulting patterns in the N. Gulf of California. (a) 3D depiction of main faults interpreted in this work from the UL9905 seismic dataset (Stock et al., 2005). Linear features correspond to main structural elements added from Bennett et al. (2013) and Martín-Barajas et al. (2013). Vertical exaggeration of the 3D projection of the fault planes is 3:1. (b) 3D depiction of the main faults in our digitized analogue model. Linear features correspond to faults which cannot be correlated across multiple cross-sections, but their presence is inferred from the model surface evolution. (c) Surface fault patterns in the N. GoC (faults in continuous lines from this work and Persaud et al., 2003, faults in dashed lines from Martín-Barajas et al., 2013, basins outlined in grey). (d) Surface fault patterns in our model. Topography and bathymetry from GMRT Grid Version 3.3 (Ryan et al., 2009). In panels (a and b), the fault plane colours are randomly generated by the interpretation software. For larger versions of the panels, refer to Figures S15–S16

Ballenas Transform Fault Zone (Figure 9a,c), which we interpret as horsetail splays of the transform zone. We consider these fault splays and the faults that define the Consag Basin (Gonzalez-Escobar et al., 2010; Persaud et al., 2003) in the north (labelled BSF in Figure 9a,c) to be the most likely basin sidewall faults. In the analogue model, an oblique-normal slip fault bounding the rear of the pull-apart depression has developed at the trailing end of the plate (Figure 9b,d BSF-B). This fault begins approximately above the rift-transform intersection point of the starting model (RTI in Figure 9d).

In the southern part of the N. GoC pull-apart structure, it appears that the role of the basin sidewall faults is played by two main faults: (a) where continental break-up is active, the basin sidewall fault is primarily defined by a long normal fault, trending parallel to the Lower Delfin Basin rift, (LDB-BSF in Figure 9c); and (b) in the east of the basin by the Cerro Prieto Sur (CPSF in Figure 9c), Amado and Adair Faults, which display both strike-slip and normal character (e.g. González-Escobar et al., 2014; Martín-Barajas et al., 2013). Similarly, in our model, a long oblique-normal slip fault defines the uppermost boundary of the pull-apart (along with two smaller structures towards the rear of the moving plate).

We also find a high degree of similarity between the transtensional PDZs in our model and the N. GoC. We exclude the southeastern part of the Ballenas Transform Fault Zone that mainly corresponds to a transform fault (south of the intersection with the Lower Delfin Basin), as we cannot replicate the creation of transform faults in our model. However, the part of the Ballenas Transform Fault Zone within the pull-apart structure displays very similar characteristics to the transtensional PDZs in our models. The main characteristic is the existence of normal faults that have accommodated rotation in their lifespan, such as the onshore Sierra San Pedro Martir normal faults in Baja California (SSPM in Figure 9b,d; Bennett et al., 2013). Similarly, in the front PDZ in our model (PDZ-F), a series of normal faults (labelled NF in Figure 9d) develops on the fixed part of the plate to accommodate the component of rotation.

Equally, in the rear parts of our model, we observe that transtensional deformation is bounded by a principal displacement zone containing a number of shorter and longer strike-slip faults (PDZ-B in Figure 9d), accompanied by faults that accommodate rotation. This agrees with observations in the northwestern part of the Cerro Prieto Fault in the Salton trough (northwest of Figure 9a,c), which is accompanied by other, smaller faults with a horizontal component (González-Escobar et al., 2020).

The rotation accommodation faults (RAFs in Figure 9b,d) in our model would most likely correspond to the faults that bound the Consag Basin (purple faults labelled BSFs in Figure 9c), since there is evidence of lateral offset in the area and their orientation also matches that of the model (Gonzalez-Escobar et al., 2010). Furthermore, part of the dextral rotation can also be accounted for by the onshore strike-slip and oblique normal faults in Sierra San Pedro Martir (SSPM on Figure 9a,c) on the Baja California Peninsula (e.g. Bennett et al., 1996; Goff et al., 1987; Humphreys & Weldon, 1991) and Sonora Areas (Darin et al., 2016).

5.1.2 | Basin morphology and sedimentation patterns

We compare the depth to the acoustic basement in the N. GoC (Figure 10a – modified from González-Escobar et al., 2014) to the depth to the top of our 3D model's pre-rift stratigraphy (Figure 10b). Both of these surfaces represent strata present before extension and rotation and thus provide good reference horizons to track the evolution of deformation. In both cases, we observe a skewed triangular depression, with the widest part between the frontal PDZ and the top BSF. This in the N. GoC would correspond to a depression delineated between the Ballenas Transform Fault Zone and the Cerro Prieto Sur Fault (Figure 10a) and in our model between the frontal PDZ and basin sidewall fault (PDZ-F and BSF-*F* (Figure 10b). This depression narrows and shallows towards the rear rift situated at the end of the rear PDZ. The rear rift in N. GoC would be represented by the Salton Trough in the NW of the pull-apart structure (outside of the map of Figure 10a). This narrower part occurs between the rear PDZ (CPF in the N. GoC and PDZ-B in our model in Figure 8a,b) and the rotation accommodation fault and rear basin sidewall faults (BSF in the N. GoC and BSF/RAF in our model in Figure 8a,b). In the case of the N. GoC, this corresponds to the Cerro Prieto Fault and the faults bounding the Consag and Wagner Basins (CPF/BSF in Figure 10a) and, in our model, to between the rear PDZ and basin sidewall/rotation accommodation faults (PDZ-B and BSF/RAF in Figure 10b). The deepest part of the depression lies close to the RTI in both cases (dark blue colour in Figure 10a,b). It is worth noting that the active PDZ during the rotation in the N. GoC was situated along the Tiburon Fault and Tiburon Basin (labelled TB in Figure 10a). Following a plate-jump at 3 Ma, the principal displacement zone migrated to its current location (Seiler et al., 2009). However even if we disregard the area containing the Upper and Lower Delfin Basins (UDB/LDB in Figure 10a) on the assumption that they did not participate in extension until after the plate jump, there is still a great degree of similarity with the model.

In Figure 10c, we show the distribution of one of the older units in the basin, the Late Miocene-Early Pliocene-aged Unit 3 (ages derived from Martín-Barajas et al., 2013), deposited near the end of the plate rotation documented in Bennett and Oskin (2014) between 12.5–6.5 Ma and the plate re-organisation occurring at 3 Ma (Lonsdale, 1989; Seiler et al., 2009).

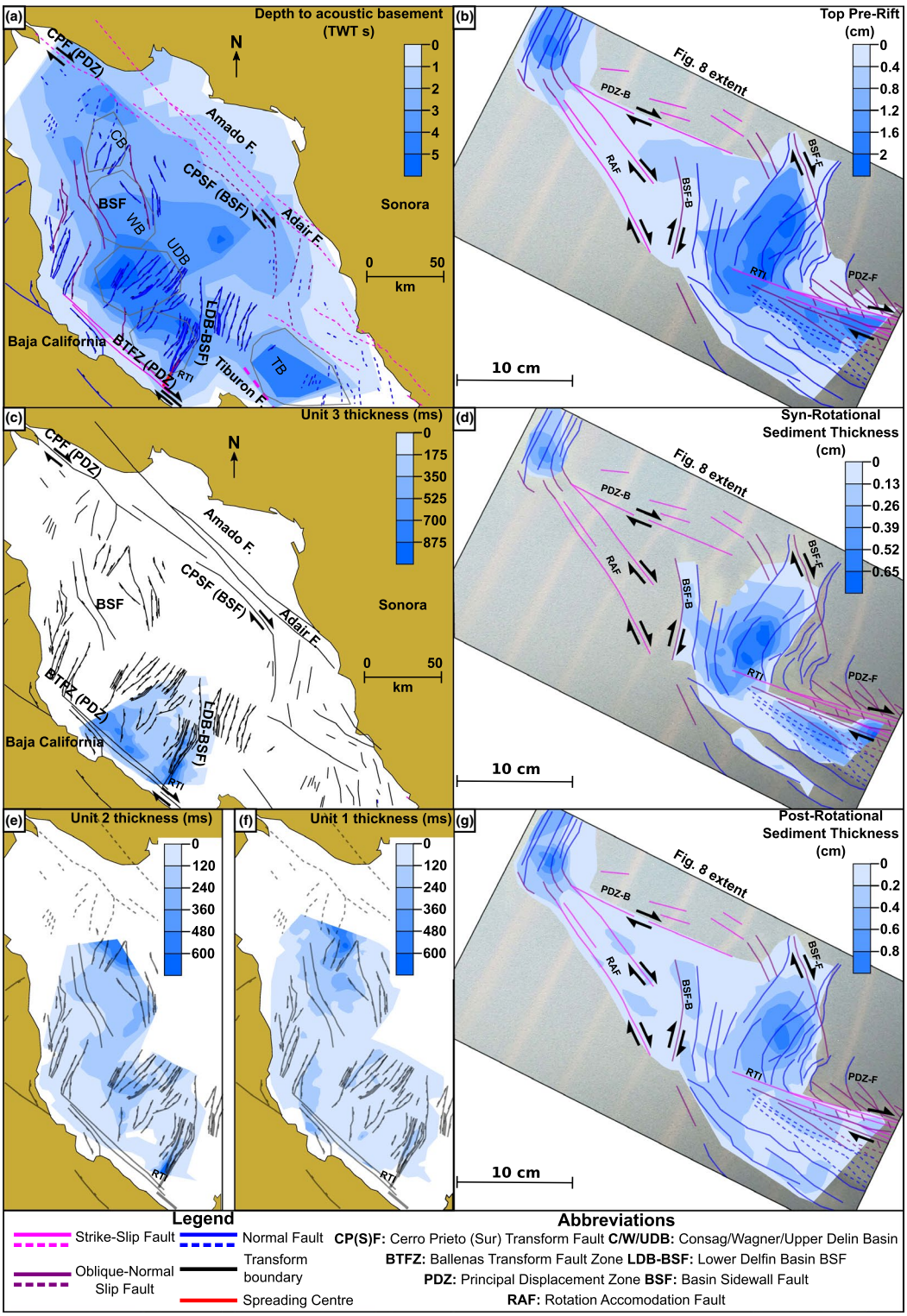

FIGURE 10 Comparison between our model and the morphology and sedimentation patterns in the N. Gulf of California. (a) Map of depth to N. Gulf of California basement (in seconds TWT, redrawn from González-Escobar et al., 2014). Basin outlines are shown in gray. (b) Map of depth to the top of the pre-rift model stratigraphy (in cm). (c) N. GoC Unit 3 thickness (in ms TWT). (d) Model syn-rotational sedimentary layer thickness (in cm). (e,f) Units 2,1 thickness (in ms TWT). (g) Model post-rotational sedimentary layer thickness (in cm). Faults and annotations are grayed out in panels (c, e and f) for clearer image view. Added sediment thickness is compared qualitatively, not quantitatively, as it is manually added to monitor depocentre focus and general sedimentation patterns

We observe that this unit has two main depocentres: one along the BTFZ-PDZ (Figure 10c) and one over the Lower Delfin Basin-basin sidewall fault rift. In both cases, sediment thickness is quite significant, in places >700 milliseconds of sediment (potentially more than 500 m). Comparing the distribution of Unit 3 to the first two syn-rift sediment units in our model (Black and Gray in Figure 6), we observe that deposition is focused in two loci: a) above the RTI and the two large faults next to the frontal basin sidewall fault (Figure 10d) which represent the basin sidewall fault during rotation and b) within the transtensional frontal PDZ. As observed in the topography map in Figure 8k, there is no significant depression over the area where the rotation accommodation faults are located, so sedimentation terminates at the rear basin sidewall fault boundary. The main depocentre is thus located closer to the main basinal depression's centre, following the trajectory of the RTI as rotation occurs.

It is important to note, however, that our observations on Unit 3 are limited by its mappable extent in the seismic dataset, due to resolution loss and the presence of volcanics that make cross-correlation of the seismic horizon across the intersecting seismic cross-sections difficult. However, we would expect the unmapped parts of Unit 3 to also behave in a similar way as the sediments in our model, since it is concurrent with the rotation in the N. GoC. Furthermore, given that the current basin configuration of the N. GoC resulted from the plate jump 3 Ma ago (Lonsdale, 1989; Seiler et al., 2009), this jump should not affect the thickness (or even presence) of these sediments in the younger basins in the Northern Gulf. The same sedimentation pattern applies to our model, where at the back there is an absence of sedimentation. Even when a plate jump is considered, Mar-Hernández et al. (2012) showed that the focus of sedimentation followed a similar pattern when the RTI migrated from the Tiburon to the Lower Delfin Basin.

Finally, we compare the sedimentation patterns across the N. GoC and our model. In the youngest two sediment layers in the N. GoC (units 2 and 1 in Figure 10e,f), as observed in this and previous work (Martín-Barajas et al., 2013; Persaud et al., 2003), the main depocentres follow the current sub-basin morphology. We regard these units as post-rotational, as they represent the youngest sequences in the basin, dated as Pleistocene (Martín-Barajas et al., 2013), and hence later than any plate re-organisation within the N. Gulf (Lonsdale, 1989). Unit 2 thickens between the BSF in the Wagner and Consag basins, but reaches its greatest thickness in the area adjacent to the active spreading centre in the Lower Delfin Basin basin sidewall fault, where the RTI is located (Figure 10e). Unit 1 (the topmost in the region) appears to be thickest in the Wagner and Consag basin area (Figure 10f). It is worth noting that in both cases no significant thickening occurs along the transform boundary of the Ballenas Transform Fault Zone (Figure 10e,f). We compare these two units to our model's top-most depositional layer (Green unit in Figure 6), which was added after rotation had finished. In our model, the highest sedimentation rate again is focused near the RTI (Figure 10g), with minor patches of thicker sediment over the rotation accommodation fault, rear PDZ and basin sidewall fault (Figure 10g, also seen in the topographic map in Figure 8l). These are areas with continuous accommodation space, as they progressively deepen once the final plate vector is established. In nature, in the later stages of the Gulf's evolution younger basins represented more depositional space, so sediment was draped over a larger area of the basin.

Examining the differences between our model and the N. GoC, we note that our model does not replicate the plate jump atca. 3 Ma (Lonsdale, 1989) that migrated the plate boundary in the N. GoC from the Tiburon Fault to the BTFZ. Therefore our model does not replicate the formation of the Gulf's younger basins. Thus, sediment distribution and depocentre migration do not follow a direct one-to-one correlation. However, there is strong evidence that the rotation established the general structural framework of the N. GoC, affecting the major structures in the area (such as the PDZ and basin sidewall faults in the east of the Gulf). If we could replicate the plate jump in our model by migrating the plate boundary towards the fixed side of the model (as seen in Figure 9d) then we would expect that the structure on the moving side of the model (as seen in Figure 9d) and any further topographic depression (representing newer basins) would occur in the fixed side as is the case in the N. GoC. Varying the rate or amount of rotation that is applied in the model or using an apparatus that would replicate the change in motion along both plates would potentially allow for an even more accurate representation of features visible in the N. GoC and a further exploration of this parameter space. Furthermore, our model does not account for the presence of magmatism such as sills and volcanic knolls in the area (Persaud et al., 2003), nor does it explore the possibility of incipient oceanic crust in the Lower Delfin Basin or Ballenas Transform Fault Zone (Persaud et al., 2003). However, the similarity between the evolution of fault and basin architecture in our model and the Gulf of California is such that we can infer that the change in relative plate motion occurring around 8 Ma (Atwater & Stock, 1998) set the initial framework for the structure of the current Northern Gulf of California.

5.2 | Comparison with the Bohai Basin in northern China

In addition to the N. GoC, our model can be compared to other transtensional basins, such as the development of the Bohai Basin in northern China.

Our model is not designed or scaled specifically to replicate the full evolution of the Bohai Basin. The basement to the Bohai Basin is thought to have a pre-existing fabric inherited from Mesozoic sinistral transpression and earlier deformation (Allen et al., 1997), while our model starts with no preexisting structural fabric (bar the velocity discontinuity created by the moving plates). Furthermore, the Bohai Basin is a basin about 1,000 km long and 600 km wide, while our model would scale to a pull-apart ~200 km long and 100 km wide. However, both the Bohai Basin and our model are transtensional basins that build on pull-apart geometries with similar length to width ratios. These first-order similarities enable us to extend the applicability of our model to this basin by (invoking similarity scaling as seen in Reber et al., 2020).

We first compare our model's top pre-rift map to the Cenozoic sediment thickness in the Bohai Basin. In both, a main depocentre exists near the PDZ-BSF intersection. In the Bohai Basin, this is the Bozhong Depression (BZHD in Figure 11a), where sedimentation has been focused since the Eocene. In our model, the main depocentre is located at the end of the triangular transtensional PDZ (darker blue parts of the main pull-apart depression in Figure 11b).

In the Bohai Basin, Allen et al. (1997) observed a number of faults in an oblique orientation with respect to the main NE-SW structural fabric, indicating dextral transtension (Figure 11a). Qi and Yang (2010) also describe the existence of transfer zones following this oblique pattern as evidence for the same transtensional movement (Figure 11a, purple faults). We find that, in our model, faults created in the later stages of rotation and after rotation is finished follow the same pattern (Figure 11b, faults labelled as BSF-B and BSF-F).

The northeastern end of the Bohai Bazin PDZ, the Liaodongwan Depression, is a 500 km long, 100 km wide transtensional PDZ with well-developed elongate basins up to 10 km deep (Figure 11a, labelled LDW Depression, and 11c). Similarly, in our model, some of the largest depositional thicknesses (bar the main pull-apart depression) can be observed at the advancing front of the frontal PDZ (darkest blue colour in PDZ-F in Figure 11b). These elongate transtensional basins are segmented by normal and oblique-normal faults, as can be seen both in map (Figure 11a, b) and cross-section view (Figure 11c, d, e). This is consistent with the observations indicating that, in transtensional PDZs, lateral slip is accommodated in broad deformation zones where the main strike-slip fault zone co-exists with oblique-normal faults at lower than 30° angles that take up part of the motion (Farangitakis et al., 2019). This is particularly clear in the cross-section view of the main PDZ of the Bohai Basin (pink and purple faults in Figure 11c). These characteristic sets of oblique-normal slip faults usually form prior to the change in rotation as pure strike-slip faults and then later evolve to a more normal (or even exclusively normal) slip character as the PDZ develops its extensional character and migrates in space (Farangitakis et al., 2019). It is worth noting that in the Liaodongwan Depression PDZ (Qi & Yang, 2010) localised compression has been observed along the strike-slip faults (Figure 11c). This deformation is distinct in timing and extent from the regional late Cenozoic basin inversion in the greater Bohai Basin area (Allen et al., 1997). In our model, a small degree of compression is also observed along the strike-slip segments of the PDZ (observed in small thickness increases on the footwalls of oblique-normal faults in layers next to the PDZ, Figure 11e, next to the left hand side strike-slip zone) even when transtension occurs, which is consistent with the anticlines next to the active strike-slip faults observed in the Bohai Basin (Figure 11c, From Qi & Yang, 2010, above the main strike-slip zone).

These observations show first-order similarity between the architecture of our model and the Bohai Basin, including the sedimentation patterns, transtensional PDZs and fault patterns. This indicates that, in addition to a later basin inversion (Qi & Yang, 2010), a rotation of extension direction has taken place during the evolution of the Bohai Basin. This transtensional event could be attributed to the NW-SE to E-W change of the convergence vector between the Pacific and Asia plates between the late Mesozoic and Early Tertiary (Engebretson et al., 1985; Liang et al., 2016).

5.3 | Further discussion

As Wu et al. (2009) note, the main difference between pure strike-slip (such as the Dead Sea basin) and transtensional pull-apart basins (such as the Gulf of Elat) is the co-existence of extension inside the PDZ and the presence of more than one depocentre in the transtensional case. Our model starts as a pure strike-slip pull-apart, proceeds into rotation and then, with a new plate motion vector, develops as a transtensional system. Basins with this multiphase development show distinct structural characteristics compared with pull-apart basins that were consistently either pure strike-slip or transtensional from the onset. The main distinguishing features from the two end-members are the migrating depocentres due to rotation (Figures 8 and 10), the Rotation Accommodation Faults (Figure 8) and the oblique-slip character of the BSFs that occur during the rotation (Figure 8). These features can be used as diagnostic tools for the identification of other natural examples where pull-apart basins have experienced multi-phase evolution. A possible further example could be the Cinarcik Basin in the Sea of Marmara, where the rotating Anatolia microplate vector has led to curvature of the North Anatolian Fault, creating transtensional pull-apart basins (Sugan et al., 2014).

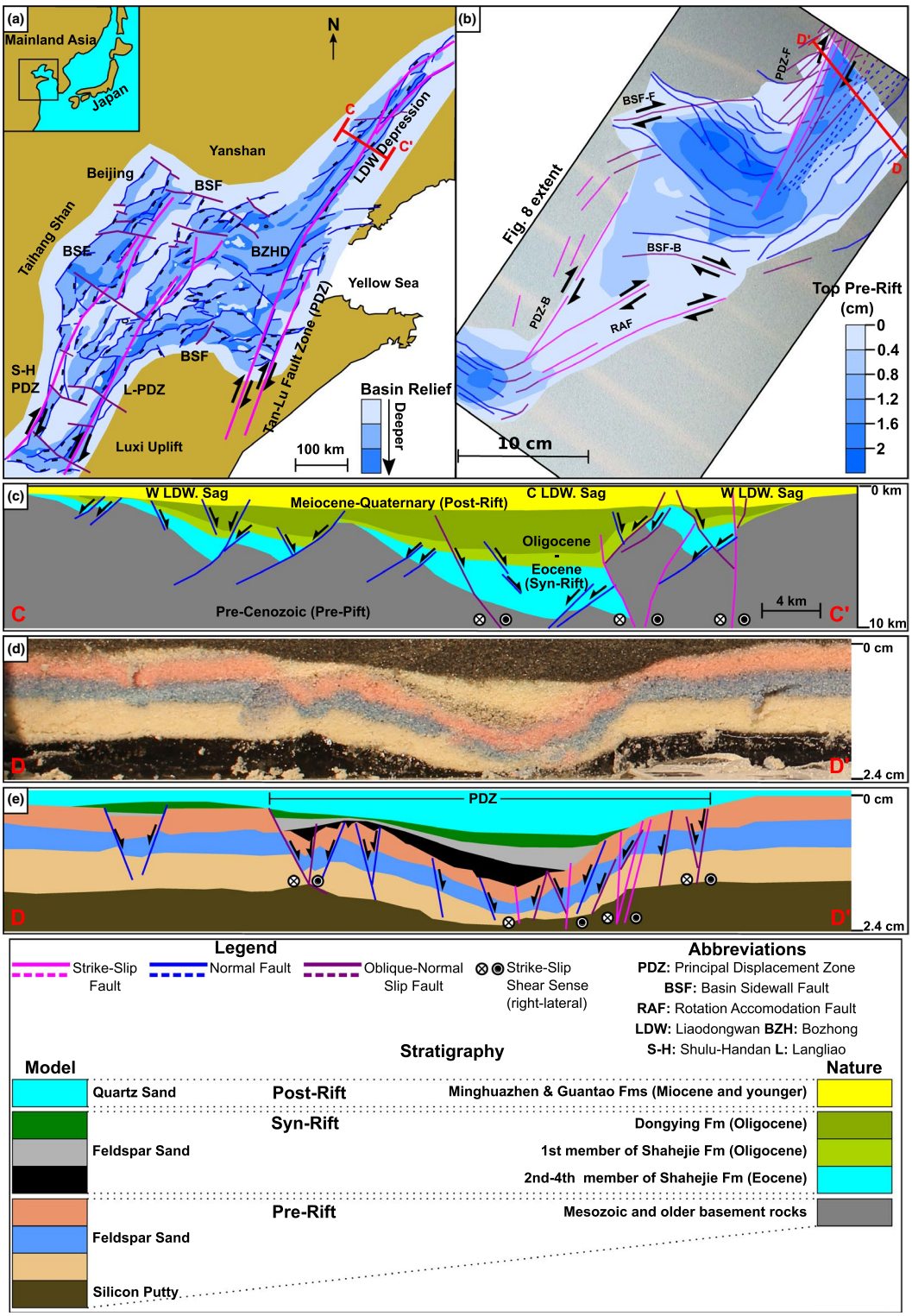

FIGURE 11 Comparison between our model and the structure of the Bohai Basin in China. (a) Map of the structure and depth to Mesozoic basement in the Bohai Basin (modified from Allen et al., 1997 and Qi & Yang, 2010). (b) Map of depth to the top of the pre-rift model stratigraphy (in cm). (c) Seismic cross-section across the Liaodongwan depression in the Bohai Basin NE PDZ (location shown in panel a, re-interpreted from Allen et al., 1998 and Qi & Yang, 2010). (d and e) Uninterpreted and interpreted cross-section across our model's front PDZ (location shown in panel b)

6 | CONCLUSIONS

We present a physical analogue model designed to simulate the effect of transtensional deformation imposed on pull-apart basins due to a change in plate motion vectors. Our model produces structural and depositional patterns that are in very good agreement with natural examples and enhance our understanding of fault geometry and development in pull-apart basins with a multiphase transtensional evolution across the world.

Our model was designed to study the setting of the northern Gulf of California and successfully reproduces the principal features of its transtensional evolution. Both the N. Gulf of California and our model develop an asymmetrical triangular pull-apart basin, bounded by strike-slip faults on either side. Both also show similar patterns of sedimentation, with pre-rotational sediments focused within the pull-apart basin's main structural elements, whilst the post-rotation sediments have a broader spatial extent, and are thickest over the younger extensional features.

Additionally, we find substantial first-order similarity between our model and the Bohai Basin in northern China, despite our model not being designed to replicate that basin's opening history or scale. In both model and nature, we observe faults oblique to the main basin trend and depocentres along the transtensional PDZ controlled by series of oblique-normal faults. These similarities support the interpretation of the Bohai Basin as a multiphase transtensional pull-apart basin, and suggest that a rotation in extension direction could have taken place during the late Mesozoic or early Tertiary, resulting in its current transtensional architecture.

Our observations indicate that the combination of features such as asymmetrical triangular pull-apart basins, migrating depocentres, wide principal displacement zones with oblique faulting and normal faults with an oblique component can be a strong indication that a pull-apart basin has undergone a transtensional rotation change due to a change in the plate motion vector along the strike-slip zones that define it.

ACKNOWLEDGEMENTS

The work contained in this paper contains work conducted during a PhD study undertaken as part of the Natural Environment Research Council (NERC) Centre for Doctoral Training (CDT) in Oil & Gas [grant number NEM00578X/1]. It is co-sponsored by Durham University, whose support is gratefully acknowledged. LMK is supported by a Royal Society of Edinburgh Personal Research Fellowship funded by the Scottish Government. The authors thank the Editor-in-Chief of Basin Research, Atle Rotevatn, and the three reviewers, Chris Morley, Hanna M Elston and Alexander Cruden, for their constructive comments which helped improve this manuscript.

PEER REVIEW

The peer review history for this article is available at https://publons.com/publon/10.1111/bre.12528.

DATA AVAILABILITY STATEMENT

The data that supports the findings of this study are available in the supplementary material of this article.

ORCID

Georgios-Pavlos Farangitakis https://orcid.org/0000-0001-6884-8444
Ken J. W. McCaffrey https://orcid.org/0000-0002-9882-1709
Ernst Willingshofer https://orcid.org/0000-0002-9119-5557
Mark B. Allen https://orcid.org/0000-0002-0656-7898
Lara M. Kalnins https://orcid.org/0000-0002-6891-0698
Jeroen van Hunen https://orcid.org/0000-0002-3050-6753
Patricia Persaud https://orcid.org/0000-0003-3462-7023
Dimitrios Sokoutis https://orcid.org/0000-0003-0523-9785

REFERENCES

Allemand, P., & Brun, J. (1991). Width of continental rifts and rheological layering of the lithosphere. *Tectonophysics*, *188*(1), 63–69. https://doi.org/10.1016/0040-1951(91)90314-I

Allen, M. B., Macdonald, D. I. M., Xun, Z., Vincent, S. J., & Brouet-Menzies, C. (1997). Early Cenozoic two-phase extension and late Cenozoic thermal subsidence and inversion of the Bohai Basin, Northern China. *Marine and Petroleum Geology*, *14*(7), 951–972. https://doi.org/10.1016/S0264-8172(97)00027-5

Allen, M. B., Macdonald, D. I. M., Xun, Z., Vincent, S. J., & Brouet-Menzies, C. (1998). Transtensional deformation in the evolution of the Bohai Basin, Northern China. *Geological Society, London, Special Publications*, *135*(1), 215–229. https://doi.org/10.1144/GSL.SP.1998.135.01.14

Armijo, R., Meyer, B., Navarro, S., King, G., & Barka, A. (2002). Asymmetric slip partitioning in the Sea of Marmara pull-apart: A clue to propagation processes of the North Anatolian Fault? *Terra Nova*, *14*(2), 80–86. https://doi.org/10.1046/j.1365-3121.2002.00397.x

Atwater, T., & Stock, J. (1998). Pacific-North America plate tectonics of the Neogene southwestern United States: An update. *International Geology Review*, *40*(5), 375–402. https://doi.org/10.1080/00206819809465216

Axen, G. (1995). Extensional segmentation of the main Gulf escarpment, Mexico and United States. *Geology*, *23*(6), 515–518. https://doi.org/10.1130/0091-7613(1995)023<0515:ESOTMG>2.3.CO;2

Basile, C., & Brun, J. P. (1999). Transtensional faulting patterns ranging from pull-apart basins to transform continental margins: An experimental investigation. *Journal of Structural Geology*, *21*(1), 23–37. https://doi.org/10.1016/S0191-8141(98)00094-7

Bennett, R. A., Rodi, W., & Reilinger, R. E. (1996). Global positioning system constraints on fault slip rates in southern California and northern Baja, Mexico. *Journal of Geophysical Research: Solid Earth*, *101*, 21943–21960. https://doi.org/10.1029/96JB02488

Bennett, S. E. K., & Oskin, M. E. (2014). Oblique rifting ruptures continents: Example from the Gulf of California shear zone. *Geology*, *42*(3), 215–218. https://doi.org/10.1130/G34904.1

Bennett, S. E. K., Oskin, M. E., & Iriondo, A. (2013). Transtensional rifting in the proto-Gulf of California near Bahia Kino, Sonora, Mexico. *GSA Bulletin*, *125*(11–12), 1752–1782. https://doi.org/10.1130/B30676.1

Brace, W., & Kohlstedt, D. (1980). Limits on lithospheric stress imposed by laboratory experiments. *Journal of Geophysical Research: Solid Earth*, *85*(B11), 6248–6252. https://doi.org/10.1029/JB085iB11p06248

Brun, J. (2002). Deformation of the continental lithosphere: Insights from brittle-ductile models. *Geological Society, London, Special Publications*, *200*(1), 355–370. https://doi.org/10.1144/GSL.SP.2001.200.01.20

Brune, S., Williams, S. E., Butterworth, N. P., & Müller, R. D. (2016). Abrupt plate accelerations shape rifted continental margins. *Nature*, *536*, 201–204. https://doi.org/10.1038/nature18319

Burchfiel, B. C., & Stewart, J. H. (1966). "Pull-Apart" origin of the central segment of Death Valley. *California. GSA Bulletin*, *77*(4), 439–442.

Burov, E. B. (2011). Rheology and strength of the lithosphere. *Marine and Petroleum Geology*, *28*(8), 1402–1443. https://doi.org/10.1016/j.marpetgeo.2011.05.008

Corti, G., & Dooley, T. P. (2015). Lithospheric-scale centrifuge models of pull-apart basins. *Tectonophysics*, *664*, 154–163. https://doi.org/10.1016/j.tecto.2015.09.004

Corti, G., Nencini, R., & Skyttä, P. (2020). Modelling the influence of pre-existing brittle fabrics on the development and architecture pull-apart basins. *Journal of Structural Geology*, *131*, 103937. https://doi.org/10.1016/j.jsg.2019.103937

Darin, M. H., Bennett, S. E. K., Dorsey, R. J., Oskin, M. E., & Iriondo, A. (2016). Late Miocene extension in coastal Sonora, México: Implications for the evolution of dextral shear in the proto-gulf of California oblique rift. *Tectonophysics*, *693*, 378–408. https://doi.org/10.1016/j.tecto.2016.04.038

Decker, K. (1996). Miocene tectonics at the Alpine-Carpathian junction and the evolution of the Vienna basin. *Mitteilungen Der Gesellschaft Der Geologie- Und Bergbaustudenten in Österreich*, *41*, 33–44.

Del Ventisette, C., Montanari, D., Sani, F., Bonini, M., & Corti, G. (2007). Reply to comment by J. Wickham on "Basin inversion and fault reactivation in laboratory experiments". *Journal of Structural Geology*, *29*(8), 1417–1418. https://doi.org/10.1016/j.jsg.2007.05.003

Dombrádi, E., Sokoutis, D., Bada, G., Cloetingh, S., & Horváth, F. (2010). Modelling recent deformation of the Pannonian lithosphere: Lithospheric folding and tectonic topography. *Tectonophysics*, *484*(1-4), 103–118. https://doi.org/10.1016/j.tecto.2009.09.014

Dorsey, R. J., & Umhoefer, P. J. (2012). Influence of sediment input and plate-motion obliquity on basin development along an active oblique-divergent plate boundary: Gulf of California and Salton trough. C. Busby & A. Azor *Tectonics of Sedimentary Basins: Recent Advances*, (209–255). Blackwell Publishing Ltd. https://doi.org/10.1002/9781444347166.ch10

Engebretson, D. C., Cox, A., & Gordon, R. G. (1985). *Relative motions between oceanic and continental plates in the Pacific Basin*, *206*). Geological Society of America.

Farangitakis, G. P., Heron, P. J., McCaffrey, K. J. W., van Hunen, J., & Kalnins, L. M. (2020). The impact of oblique inheritance and changes in relative plate motion on the development of rift-transform systems. *Earth and Planetary Science Letters*, *541*, 116277. https://doi.org/10.1016/j.epsl.2020.116277

Farangitakis, G.-P., Sokoutis, D., McCaffrey, K. J. W., Willingshofer, E., Kalnins, L. M., Phethean, J. J. J., Hunen, J., & Steen, V. (2019). Analogue modeling of plate rotation effects in transform margins and rift-transform intersections. *Tectonics*, *38*(3), 823–841. https://doi.org/10.1029/2018TC005261

Feng, D., & Ye, F. (2018). Structure kinematics of a transtensional basin: An example from the Llinnan subsag, Bohai Bay basin, Eastern China. *Geoscience Frontiers*, *9*(3), 917–929. https://doi.org/10.1016/j.gsf.2017.05.012

Goff, J. A., Bergman, E. A., & Solomon, S. C. (1987). Earthquake source mechanisms and transform fault tectonics in the Gulf of California. *Journal of Geophysical Research: Solid Earth*, *92*, 10485–10510. https://doi.org/10.1029/JB092iB10p10485

González-Escobar, M., Mares Agüero, M. A., & Martin, A. (2020). Subsurface structure revealed by seismic reflection images to the southwest of the Cerro Prieto pull-apart basin, Baja California. *Geothermics*, *85*, 101779. https://doi.org/10.1016/j.geothermics.2019.101779

Gonzalez-Escobar, M., Suarez-Vidal, F., Hernandez-Perez, J. A., & Martin-Barajas, A. (2010). Seismic reflection-based evidence of a transfer zone between the Wagner and Consag basins: Implications for defining the structural geometry of the northern Gulf of California. *Geo-Marine Letters*, *30*(6), 575–584. https://doi.org/10.1007/s00367-010-0204-0

González-Escobar, M., Suárez-Vidal, F., Sojo-Amezquita, A., Gallardo-Mata, C. G., & Martin-Barajas, A. (2014). Consag basin: Northern Gulf of California, evidence of generation of new crust, based on seismic reflection data. *International Geology Review*, *56*(11), 1315–1331. https://doi.org/10.1080/00206814.2014.941023

Guo, X., Wu, Z., Yang, X., Xu, H., Zhang, Z., Shi, X., & Sun, Z. (2009). The evolution of transtensional structure and numerical modeling of stress field, linnan subsag, bohai bay basin. *Marine Geology & Quaternary Geology*, *29*(6), 75–82. https://doi.org/10.1007/s12517-017-2850-2

Hu, S., O'Sullivan, P. B., Raza, A., & Kohn, B. P. (2001). Thermal history and tectonic subsidence of the Bohai Basin, Northern China: A Cenozoic rifted and local pull-apart basin. *Physics of the Earth and Planetary Interiors*, *126*(3), 221–235. https://doi.org/10.1016/S0031-9201(01)00257-6

Hubbert, M. K. (1937). Theory of scale models as applied to the study of geologic structures. *GSA Bulletin*, *48*(10), 1459–1520. https://doi.org/10.1130/gsab-48-1459

Humphreys, E. D., & Weldon, R. J. II (1991). Kinematic constraints on the rifting of Baja California. In J. P. Dauphin & B. R. T. Simoneit (Eds.), *The gulf and peninsular provinces of the californias* (pp. 217–228). AAPG Memoirs.

Klimetz, M. P. (1983). Speculations on the Mesozoic plate tectonic evolution of Eastern China. *Tectonics*, *2*(2), 139–166. https://doi.org/10.1029/TC002i002p00139

Lee, E. Y., & Wagreich, M. (2017). Polyphase tectonic subsidence evolution of the Vienna basin inferred from quantitative subsidence analysis of the northern and central parts. *International Journal of Earth Sciences (Geologische Rundschau)*, *106*(2), 687–705. https://doi.org/10.1007/s00531-016-1329-9

Liang, J., Wang, H., Bai, Y., Ji, X., & Duo, X. (2016). Cenozoic tectonic evolution of the bohai bay basin and its coupling relationship with pacific plate subduction. *Journal of Asian Earth Sciences*, *127*, 257–266. https://doi.org/10.1016/j.jseaes.2016.06.012

Liangjie, T., Guimei, W., & Xinhuai, Z. (2008). Cenozoic geotectonic evolution of the bohai basin. *Geological Journal of China Universities*, *14*(2), 191–198.

Lizarralde, D., Axen, G. J., Brown, H. E., Fletcher, J. M., González-Fernández, A., Harding, A. J., Holbrook, W. S., Kent, G. M., Paramo, P., Sutherland, F., & Umhoefer, P. J. (2007). Variation in styles of rifting in the Gulf of California. *Nature*, *448*(7152), 466–469. https://doi.org/10.1038/nature06035

Lonsdale, P. (1989). Geology and tectonic history of the Gulf of California. In E. L. Winterer, D. M. Hussong, & R. W. Decker (Eds.), *The eastern Pacific Ocean and Hawaii, geology of North America* (pp. 499–521). Geological Society of America.

Luth, S., Willingshofer, E., Sokoutis, D., & Cloetingh, S. (2010). Analogue modelling of continental collision: Influence of plate coupling on mantle lithosphere subduction, crustal deformation and surface topography. *Tectonophysics*, *484*(1), 87–102. https://doi.org/10.1016/j.tecto.2009.08.043

Mann, P. (2007). Global catalogue, classification and tectonic origins of restraining- and releasing bends on active and ancient strike-slip fault systems. *Geological Society, London, Special Publications*, *290*(1), 13–142. https://doi.org/10.1144/SP290.2

Mar-Hernández, E., González-Escobar, M., & Martin-Barajas, A. (2012). Tectonic framework of Tiburon basin, Gulf of California, from seismic reflection evidence. *International Geology Review*, *54*(11), 1271–1283. https://doi.org/10.1080/00206814.2011.636988

Martín-Barajas, A., González-Escobar, M., Fletcher, J. M., Pacheco, M., Oskin, M., & Dorsey, R. (2013). Thick deltaic sedimentation and detachment faulting delay the onset of continental rupture in the northern Gulf of California: Analysis of seismic reflection profiles. *Tectonics*, *32*(5), 1294–1311. https://doi.org/10.1002/tect.20063

McClay, K., & Dooley, T. (1995). Analogue models of pull-apart basins. *Geology*, *23*(8), 711–714. https://doi.org/10.1130/0091-7613(1995)023<0711:AMOPAB>2.3.CO;2

Morley, C. (2017). Cenozoic rifting, passive margin development and strike-slip faulting in the Andaman sea: A discussion of established v. new tectonic models. *Geological Society, Londons Memoirs*, *47*(1), 27–50. https://doi.org/10.1144/M47.4

Morley, C., & Alvey, A. (2015). Is spreading prolonged, episodic or incipient in the Andaman Sea? Evidence from deepwater sedimentation. *Journal of Asian Earth Sciences*, *98*, 446–456. https://doi.org/10.1016/j.jseaes.2014.11.033

Morley, C. K., & Searle, M. (2017). Regional tectonics, structure and evolution of the Andaman-Nicobar islands from ophiolite formation and obduction to collision and back-arc spreading. *Geological Society, London, Memoirs*, *47*(1), 51–74. https://doi.org/10.1144/M47.5

Persaud, P., Di Luccio, F., & Clayton, R. W. (2015). Rayleigh wave dispersion measurements reveal low-velocity zones beneath the new crust in the Gulf of California. *Geophysical Research Letters*, *42*(6), 1766–1774. https://doi.org/10.1002/2015GL063420

Persaud, P., Pérez-Campos, X., & Clayton, R. W. (2007). Crustal thickness variations in the margins of the Gulf of California from receiver functions. *Geophysical Journal International*, *170*(2), 687–699. https://doi.org/10.1111/j.1365-246X.2007.03412.x

Persaud, P., Stock, J. M., Steckler, M. S., Martín-Barajas, A., Diebold, J. B., González-Fernández, A., & Mountain, G. S. (2003). Active deformation and shallow structure of the Wagner, Consag, and Delfín basins, northern Gulf of California, Mexico. *Journal of Geophysical Research: Solid Earth*, *108*(B7), 2355. https://doi.org/10.1029/2002JB001937

Persaud, P., Tan, E., Contreras, J., & Lavier, L. (2017). A bottom-driven mechanism for distributed faulting in the Gulf of California rift. *Tectonophysics*, *719–720*, 51–65. https://doi.org/10.1016/j.tecto.2016.11.024

Qi, J., & Yang, Q. (2010). Cenozoic structural deformation and dynamic processes of the Bohai Bay Basin province. *China. Marine and Petroleum Geology*, *27*(4), 757–771. https://doi.org/10.1016/j.marpetgeo.2009.08.012

Rahe, B., Ferrill, D. A., & Morris, A. P. (1998). Physical analog modeling of pull-apart basin evolution. *Tectonophysics*, *285*(1), 21–40. https://doi.org/10.1016/S0040-1951(97)00193-5

Ramberg, H. (1981). *Gravity, deformation, and the earth's crust: In theory, experiments and geological application*. Academic press.

Reber, J. E., Cooke, M. L., & Dooley, T. P. (2020). What model material to use? A review on rock analogs for structural geology and tectonics. *Earth-Science Reviews*, *202*, 103107. https://doi.org/10.1016/j.earscirev.2020.103107

Ryan, W. B. F., Carbotte, S. M., Coplan, J. O., O'Hara, S., Melkonian, A., Arko, R., Weissel, R. A., Ferrini, V., Goodwillie, A., Nitsche, F., Bonczkowski, J., & Zemsky, R. (2009). Global multi-resolution topography synthesis. *Geochemistry, Geophysics, Geosystems*, *10*(3). https://doi.org/10.1029/2008GC002332

Seiler, C., Gleadow, A. J. W., Fletcher, J. M., & Kohn, B. P. (2009). Thermal evolution of a sheared continental margin: Insights from the Ballenas transform in Baja California, Mexico. *Earth and Planetary Science Letters*, *285*(1–2), 61–74. https://doi.org/10.1016/j.epsl.2009.05.043

Sims, D., Ferrill, D. A., & Stamatakos, J. A. (1999). Role of a ductile décollement in the development of pull-apart basins: Experimental results and natural examples. *Journal of Structural Geology*, *21*(5), 533–554. https://doi.org/10.1016/S0191-8141(99)00010-3

Smit, J., Brun, J.-P., Fort, X., Cloetingh, S., & Ben-Avraham, Z. (2008). Salt tectonics in pull-apart basins with application to the Dead Sea Basin. *Tectonophysics*, *449*(1), 1–16. https://doi.org/10.1016/j.tecto.2007.12.004

Sokoutis, D., Bonini, M., Medvedev, S., Boccaletti, M., Talbot, C. J., & Koyi, H. (2000). Indentation of a continent with a built-in thickness change: experiment and nature. *Tectonophysics*, *320*(3-4), 243–270. https://doi.org/10.1016/S0040-1951(00)00043-3

Sokoutis, D., Burg, J., Bonini, M., Corti, G., & Cloetingh, S. (2005). Lithospheric-scale structures from the perspective of analogue continental collision. *Tectonophysics*, *406*(1), 1–15. https://doi.org/10.1016/j.tecto.2005.05.025

Srisuriyon, K., & Morley, C. (2014). Pull-apart development at overlapping fault tips: Oblique rifting of a Cenozoic continental margin, northern Mergui basin, Andaman Sea. *Geosphere*, *10*(1), 80–106. https://doi.org/10.1130/GES00926.1

Stock, J., & Hodges, K. (1989). Pre-Pliocene extension around the Gulf of California and the transfer of Baja California to the Pacific Plate. *Tectonics*, *8*(1), 99–115. https://doi.org/10.1029/TC008i001p00099

Stock, J., Mountain, G., Diebold, J., Steckler, M., & Martin-Barajas, A. (2005). HiRes Multi-Channel Seismic Shot Data from the Northern Gulf of California acquired during the R/V Francisco de Ulloa expedition UL9905 (1999). *Integrated Earth Data Applications (IEDA)*. https://doi.org/10.1594/IEDA/303735

Sugan, M., Wu, J., & McClay, K. (2014). 3D analogue modelling of transtensional pull-apart basins: Comparison with the Cinarcik Basin, Sea of Marmara, Turkey. *Bollettino Di Geofisica Teorica Ed Applicata*, *55*(4), 699–716.

Tchalenko, J. S. (1970). Similarities between shear zones of different magnitudes. *GSA Bulletin*, *81*(6), 1625–1940.

ten Brink, U. S., Katzman, R., & Lin, J. (1996). Three-dimensional models of deformation near strike-slip faults. *Journal of Geophysical Research: Solid Earth*, *101*, 16205–16220. https://doi.org/10.1029/96JB00877

Tron, V., & Brun, J.-P. (1991). Experiments on oblique rifting in brittle-ductile systems. *Tectonophysics*, *188*(1-2), 71–84. https://doi.org/10.1016/0040-1951(91)90315-J

Umhoefer, P. J., Darin, M. H., Bennett, S. E. K., Skinner, L. A., Dorsey, R. J., & Oskin, M. E. (2018). Breaching of strike-slip faults and successive flooding of pull-apart basins to form the Gulf of California seaway from ca. 8–6 ma. *Geology*, *46*(8), 695–698. https://doi.org/10.1130/G40242.1

van Wijk, J., Axen, G., & Abera, R. (2017). Initiation, evolution and extinction of pull-apart basins: Implications for opening of the Gulf of California. *Tectonophysics*, *719–720*, 37–50. https://doi.org/10.1016/j.tecto.2017.04.019

Weijermars, R. (1986a). Flow behaviour and physical chemistry of bouncing putties and related polymers in view of tectonic laboratory applications. *Tectonophysics*, *124*(3), 325–358. https://doi.org/10.1016/0040-1951(86)90208-8

Weijermars, R. (1986b). Polydimethylsiloxane flow defined for experiments in fluid dynamics. *Applied Physics Letters*, *48*(2), 109–111. https://doi.org/10.1063/1.97008

Weijermars, R. (1986c). Finite strain of laminar flows can be visualized in SGM36-polymer. *Naturwissenschaften*, *73*(1), 33–34. https://doi.org/10.1007/bf01168803

Weijermars, R., & Schmeling, H. (1986). Scaling of newtonian and non-newtonian fluid dynamics without inertia for quantitative modelling of rock flow due to gravity (including the concept of rheological similarity). *Physics of the Earth and Planetary Interiors*, *43*(4), 316–330. https://doi.org/10.1016/0031-9201(86)90021-X

Wickham, J. (2007). Comment on "Basin inversion and fault reactivation in laboratory experiments". *Journal of Structural Geology*, *29*(8), 1414–1416. https://doi.org/10.1016/j.jsg.2007.05.002

Willingshofer, E., Sokoutis, D., Beekman, F., Schönebeck, J.-M., Warsitzka, M., & Rosenau, M. (2018). Ring shear test data of feldspar sand and quartz sand used in Tectonic Laboratory (TecLab) at Utrecht University for experimental Earth Science applications. *GFZ Data Services., V.1. GFZ Data Services*. https://doi.org/10.5880/fidgeo.2018.072

Willingshofer, E., Sokoutis, D., & Burg, J. P. (2005). Lithospheric scale analogue modelling of collision zones invoking a pre-existing weak zone. In "Deformation Mechanisms, Rheology and Tectonics: From Minerals to the Lithosphere" (Eds. Gapais D., Brun J.P. & Cobbold P.R.). *Geological Society, London, Special Publications*, *243*, 277–294.

Withjack, M. O., & Jamison, W. R. (1986). Deformation produced by oblique rifting. *Tectonophysics*, *126*(2), 99–124. https://doi.org/10.1016/0040-1951(86)90222-2

Wu, J. E., McClay, K., Whitehouse, P., & Dooley, T. (2009). 4D analogue modelling of transtensional pull-apart basins. *Marine and Petroleum Geology*, *26*(8), 1608–1623. https://doi.org/10.1016/j.marpetgeo.2008.06.007

SUPPORTING INFORMATION

Additional Supporting Information may be found online in the Supporting Information section.

How to cite this article: Farangitakis G, McCaffrey KJW, Willingshofer E, et al. The structural evolution of pull-apart basins in response to changes in plate motion. *Basin Res*. 2021;33:1603–1625. https://doi.org/10.1111/bre.12528